

Autophagy-dependent TOR reactivation drives fungal growth in living host rice cells

Gang Li

University of Nebraska-Lincoln

Ziwen Gong

University of Nebraska-Lincoln

Nawaraj Dulal

University of Nebraska-Lincoln

Raquel Rocha

University of Nebraska-Lincoln <https://orcid.org/0000-0003-3264-2385>

Richard Wilson (✉ rwilson10@unl.edu)

University of Nebraska-Lincoln <https://orcid.org/0000-0002-7754-7712>

Article

Keywords: Rice blast disease, Magnaporthe oryzae, biotrophy, biotrophic interface, Rim15, autophagy, TOR signaling, GFP-ATG8, glutaminolysis, GS-GOGAT, α -ketoglutarate, prototrophy

Posted Date: March 2nd, 2022

DOI: <https://doi.org/10.21203/rs.3.rs-1344614/v1>

License:  This work is licensed under a Creative Commons Attribution 4.0 International License.

[Read Full License](#)

1 **Autophagy-dependent TOR reactivation drives fungal growth in living host rice**
2 **cells**

3 **Gang Li¹, Ziwen Gong^{1,2}, Nawaraj Dulal, Raquel O. Rocha and Richard A. Wilson***

4 **Department of Plant Pathology, University of Nebraska-Lincoln, Lincoln, NE, USA**

5 ¹Contributed equally

6 ²Current address: State Key Laboratory for Biology of Plant Diseases and Insect Pests, Institute of Plant
7 Protection, Chinese Academy of Agricultural Sciences, Beijing, China

8 *rwilson10@unl.edu

9 **Abstract**

10 The devastating blast fungus *Magnaporthe oryzae* elaborates invasive hyphae (IH) in living rice cells,
11 separated from host cytoplasm by plant-derived interfacial membranes, but the molecular mechanisms
12 and metabolic strategies (and hence metabolic vulnerabilities) underpinning this fundamental intracellular
13 biotrophic growth phase are poorly understood. Eukaryotic cell growth depends on activated target-of-
14 rapamycin (TOR) kinase signaling, which inhibits autophagy. Here, using live-cell imaging coupled with
15 multiomic approaches, we show how cycles of autophagy in IH modulate TOR reactivation via α-
16 ketoglutarate to support biotrophic growth. Deleting the *M. oryzae* serine-threonine protein kinase-
17 encoding gene *RIM15* abolished the *in planta* autophagic cycling we describe here in wild type,
18 attenuating biotrophic growth and disrupting interfacial membrane integrity. $\Delta rim15$ biotrophic growth was
19 remediated by α-ketoglutarate treatment. Altogether, our results demonstrate that Rim15-dependent
20 cycles of autophagic flux liberate α-ketoglutarate – via glutaminolysis – as an amino acid-sufficiency
21 signal to trigger TOR reactivation and promote biotrophic growth in host rice cells.

22 **Key words:** Rice blast disease, *Magnaporthe oryzae*, biotrophy, biotrophic interface, Rim15, autophagy,
23 TOR signaling, GFP-ATG8, glutaminolysis, GS-GOGAT, α-ketoglutarate, prototrophy

24 **Introduction**

25 *Magnaporthe oryzae* (syn *Pyricularia oryzae*)¹ causes blast, the most devastating disease of cultivated
26 rice²⁻⁴. *M. oryzae* is a hemibiotroph, an important class of eukaryotic microbial plant pathogen that,
27 following host invasion, grows undetected as a biotroph for an extended period in living host plant cells
28 before switching to necrotrophy, when host cells die and disease symptoms develop. In many
29 pathosystems, biotrophic growth involves the elaboration of feeding structures (haustorium) or
30 intracellular invasive hyphae (IH) that are surrounded by host plant-derived membranes to form interfacial
31 zones for nutrient acquisition and the deployment of plant innate immunity-suppressing effectors⁵. The *M.*
32 *oryzae* biotrophic interface comprises IH wrapped in the plant-derived extra-invasive hyphal membrane

33 (EIHM), forming an interfacial compartment into which apoplastic effectors like Bas4 can be deployed^{6,7}.
34 *M. oryzae* IH also associate with a focal plant lipid-rich structure called the biotrophic interfacial complex
35 (BIC). A single BIC forms in the first infected rice cell following penetration at around 28-32 hr post
36 inoculation (hpi) and at the tips of IH as they spread into neighbouring cells at around 44 hpi. BICs form
37 outside IH and accumulate secreted cytoplasmic effectors such as Pwl2 before they are translocated into
38 the host cell^{6,7}. In addition to effectors, fungal antioxidation systems are essential to the success of
39 biotrophic invasion by scavenging host reactive oxygen species (ROS) that otherwise trigger plant innate
40 immunity⁸⁻¹¹. Despite being essential for disease progression, and although well described at the cellular
41 level^{7,12}, very little is known at the molecular level about plant-pathogen interfacial biology, including its
42 integration with biotrophic growth¹³. Consequently, important molecular details regarding the basic
43 principles of plant-microbe interactions are obscured.

44 We seek to understand the metabolic strategies and molecular decision-making processes employed by
45 *M. oryzae* to ensure metabolic homeostasis during biotrophy, when resources must be allocated between
46 IH growth, maintaining interfacial integrity, and plant defense suppression. How fungal metabolic
47 homeostasis is achieved during biotrophy is particularly intriguing when considering that genetic studies
48 indicate fungal acquisition of host purines and amino acids is severely limited or non-existent during
49 biotrophy¹⁴⁻¹⁶. Recently, we uncovered a role for the *M. oryzae* target-of-rapamycin (TOR) signaling
50 pathway in mediating biotrophic growth, maintaining biotrophic interface integrity (despite the plant origins
51 of BIC and EIHM membranes) and ensuring correct effector deployment¹³. TOR kinase is a conserved
52 signaling hub that promotes growth in the presence of nutrients and energy and induces autophagy under
53 starvation conditions¹⁷. In a forward genetics screen, we identified a vacuole membrane protein, Imp1, as
54 a downstream TOR signaling component required for autophagy induction¹³. $\Delta imp1$ mutant strains
55 penetrated leaf cuticles using functional appressoria, and developed IH with one or two branches, but IH
56 failed to fill the first infected rice cell and $\Delta imp1$ BICs and the EIHM eroded¹³. $\Delta imp1$ biotrophic growth
57 and interfacial integrity was restored by treatment with the TOR-independent autophagy inducer
58 amiodarone hydrochloride (AM), while treatment of WT-infected rice cells with the autophagy inhibitor 3-
59 methyladenine (3-MA) recapitulated the $\Delta imp1$ phenotype. We concluded that TOR-Imp1-autophagy
60 signaling maintains membrane homeostasis via phagophore expansion to prevent interfacial erosion and
61 thus support biotrophic growth¹³.

62 To understand more about the molecular underpinnings of biotrophic growth, here, we screened genes
63 for roles in maintaining biotrophic interfacial integrity by expressing Pwl2-mCherry^{NLS} and Bas4-GFP as
64 fluorescent biotrophic membrane integrity probes in two mutant strains impaired for biotrophic growth: a
65 mutant strain disrupted for the *M. oryzae* homologue of *RIM15* encoding a serine-threonine protein kinase
66 that in yeast acts on autophagy in parallel with TORC1¹⁸⁻²¹; and $\Delta asn1$, a previously characterized
67 asparagine auxotrophic mutant unable to establish biotrophic growth¹⁶. Examining these mutant strains
68 using a combination of live-cell imaging, leaf sheath infusions of glutamine-related metabolites and

69 autophagy modifiers, genome-wide RNAseq, proteomic, quantitative phosphoproteomic and metabolomic
70 approaches, and plate tests, revealed that biotrophic growth and interfacial membrane integrity requires
71 cycles of autophagy-dependent TOR reactivation mediated by α-ketoglutarate, a previously unknown
72 amino acid sufficiency signal (**Fig. 1a**). By delivering new insights into the fundamental nature and
73 regulation of fungal biotrophic growth, and how fungal metabolism is integrated with host plant cell innate
74 immunity suppression, this work lays a more solid foundation for comprehensively understanding
75 pathogen colonization of living host cells at the systems biology level.

76 **Results**

77 **The serine/threonine protein kinase Rim15 is required for biotrophic growth and interfacial 78 membrane integrity**

79 The serine/threonine protein kinase Rim15 is well characterized in yeast and functions to integrate
80 signaling from the nutrient-sensing kinases TORC1, Sch9, PKA and Pho85-Pho80. Yeast Rim15 is
81 required for starvation-induced autophagy in response to PKA and Sch9 inactivation, but it is not required
82 for TORC1-dependent rapamycin-induced autophagy, suggesting PKA and Sch9 in yeast regulate
83 autophagy in a pathway parallel to the TORC1 pathway¹⁸⁻²¹. The blast fungus gene MGG_00345²² is the
84 *M. oryzae* *RIM15* homologue. Using this sequence, we disrupted the *RIM15* coding region in our WT
85 Guy11 isolate using homologous gene recombination to replace the first 1 kb of the *RIM15* coding
86 sequence with the *ILV2* gene conferring sulphonylurea resistance¹³. More than ten *Δrim15*-carrying
87 mutant strains were identified by PCR and two deletants, *Δrim15* #7 and #9, were initially characterized
88 and found to be indistinguishable (**Fig. 1b,c** and **Supplementary Fig. 1a-d**). *Δrim15* #7 was used as the
89 recipient for the *RIM15-GFP* gene to generate the *Δrim15 RIM15-GFP* complementation strain (**Fig. 1b**).
90 *Δrim15* #7 was also the recipient of the pBV591 vector⁶ to generate a *Δrim15*-carrying mutant strain
91 producing Pwl2-mCherry^{NLS} and Bas4-GFP (**Fig. 1d**). Compared to the WT parental strain, *Δrim15* #7 and
92 #9 deletion strains were marginally reduced in radial diameter on complete media (CM), and both were
93 reduced for sporulation on CM (**Supplementary Fig. 1a,b**). Sporulation was improved on oatmeal agar,
94 enabling enough *Δrim15* spores to be harvested for downstream applications. Applying equal numbers of
95 spores to 3-week-old seedlings of the susceptible CO-39 rice cultivar showed that compared to WT and
96 the complementation strain, *Δrim15* #7 and #9 mutant strains were non-pathogenic, with both deletants
97 producing only small, Type I lesions²³ that did not produce spores. Thus, *RIM15* is required for
98 pathogenicity.

99 *Δrim15* #7 and #9 formed normal-looking appressoria that were melanized and inflated on artificial
100 hydrophobic surfaces by 24 hpi (**Supplementary Fig. 1c**). *Δrim15* #7 and #9 appressoria formed at rates
101 that were indistinguishable from WT on both hydrophobic surfaces and detached rice leaf sheath surfaces
102 (**Supplementary Fig. 1d**), and *Δrim15* #7 and #9 appressoria penetrated rice leaf sheaths at rates
103 comparable to WT (**Supplementary Fig. 1d**). However, although able to elaborate IH in the first infected

104 cell, subsequent growth was curtailed compared to WT (**Fig. 1c**). By 44 hpi, $\Delta rim15$ #7 and #9 IH
105 movement into adjacent cells (which occurs via plasmodesmata^{12,24}) was rarely observed
106 (**Supplementary Fig. 1d**) and if so, it only involved one or two IH strands that failed to grow far into the
107 second infected cell (eg see **Fig. 2b**). We conclude that *RIM15* is required for establishing extensive
108 biotrophic growth in the first infected rice cell.

109 We next employed our $\Delta rim15$ strain carrying *PWL2-mCherry^{NLS}* and *BAS4-GFP* to determine if
110 attenuated $\Delta rim15$ biotrophic growth impacted interfacial membrane integrity. By 36 hpi, in the control
111 *RIM15*⁺ strain, *Pwl2-mCherry^{NLS}* accumulated in the BIC and *Bas4-GFP* accumulated in the apoplastic
112 space to outline IH, as previously described^{6,7,9,13} (**Fig. 1d**). Similarly, although $\Delta rim15$ IH was already
113 impaired for growth by 36 hpi compared to WT, we nonetheless observed in most $\Delta rim15$ -infected rice
114 cells that *Pwl2-mCherry^{NLS}* accumulated in prominent BICs and the EIHM was intact resulting in *Bas4-*
115 *GFP* accumulation in the apoplast (**Fig. 1d**). However, about 4 % of $\Delta rim15$ -infected rice cells displayed
116 some *Bas4-GFP* leakage into the host cytoplasm. By 39 hpi, when all WT-infected rice cells displayed
117 intact BICs and EIHM, over half of all $\Delta rim15$ -infected rice cells (n=50, repeated in triplicate) had lost BICs
118 and were leaking *Bas4-GFP* into the cytoplasm, indicating BIC and EIHM integrity was lost (**Fig. 2a**). This
119 is similar to what was observed for $\Delta imp1$ strains¹³. By 44 hpi (**Fig. 2b**), all $\Delta rim15$ -infected rice cells had
120 lost their BICs and *Bas4-GFP* was observed in the rice cytoplasm in some cases, but this was often
121 obscured by very robust plant defense responses that manifested as granules in the host cell. Such a
122 strong host cell response was not observed for $\Delta imp1$ -infected rice cells¹³. Together, these results
123 indicated that *RIM15* was not required for establishing IH growth and biotrophic interfacial membrane
124 integrity but was, like *IMP1*, required for maintaining biotrophic interfacial membrane integrity and
125 supporting sustained IH growth. Moreover, because, by 44 hpi, $\Delta rim15$ -infected rice cells elicited an
126 extremely robust host plant defense response (**Fig. 2b**) – proceeded by the accumulation of host ROS at
127 30 hpi (**Supplementary Fig. 1e**) – that was not observed for $\Delta imp1$ -infected rice cells¹³, we concluded
128 from these first experiments that Rim15 acted in the TOR-Imp1-autophagy signaling cascade downstream
129 of TOR but upstream of Imp1 at a branch with a separate Rim15-controlled pathway mediating ROS
130 scavenging and host innate immunity suppression.

131 In support of our hypothesis of an epistatic TOR-Rim15-Imp1-autophagy-biotrophic growth pathway (with
132 a separate Rim15-ROS scavenging/host innate immunity suppression branch), **Fig. 3a** shows that, like for
133 $\Delta imp1$ ¹³, the $\Delta rim15$ mutant strain was impaired in autophagy and grew poorly on starvation media
134 compared to WT. Also, like $\Delta imp1$ ¹³, $\Delta rim15$ biotrophic growth and interfacial membrane integrity was
135 remediated by 44 hpi following treatment of $\Delta rim15$ -infected rice leaf sheaths at 36 hpi with the autophagy
136 stimulator AM (**Fig. 3b**). However, unlike $\Delta imp1$, which was unresponsive to rapamycin treatment¹³,
137 $\Delta rim15$ biotrophic interfacial integrity was remediated by rapamycin treatment (although rapamycin
138 treatment attenuated biotrophic growth for both *RIM15*⁺ and $\Delta rim15$ strains) (**Fig. 3b**). Therefore, we

139 rejected our hypothesis of a linear relationship between TOR, Rim15 and Imp1 and instead proposed
140 that, like in yeast (where Rim15 is also not required for rapamycin-induced responses), Rim15 acts on
141 autophagy in parallel with the TOR-autophagy signaling axis (**Fig. 3c**).

142 **Rim15 mediates autophagic flux during vegetative and biotrophic growth**

143 To further elaborate the role of *RIM15* in biotrophic growth, we next focused on its connection to
144 autophagy. To understand specifically how autophagy was affected in $\Delta rim15$ strains, we constructed a
145 plasmid encoding GFP fused to the N-terminus of *M. oryzae* autophagy-related protein 8 (Atg8) and
146 transformed it into WT and $\Delta rim15$ #7 to perform the GFP-Atg8 processing assay for bulk autophagic
147 activity²⁵ (**Fig. 4a**). In this assay, autophagy activity results in autophagic bodies carrying GFP-Atg8 fusing
148 with the vacuole, where Atg8 is degraded following lysis of the autophagic body, but GFP is more
149 resistant to proteolysis and thus accumulates^{19,21,25}. For each strain carrying *GFP-ATG8*, two independent
150 transformants were analyzed and found to have identical phenotypes with regards to GFP-Atg8
151 localization. **Fig. 4b** shows that in *RIM15⁺*, as expected, little or no autophagic activity was detected in
152 vegetative mycelia in CM, with GFP-ATG8 accumulating in the cytoplasm and no GFP in vacuoles,
153 whereas under nutrient-starvation conditions, GFP accumulated in vacuoles. In contrast, $\Delta rim15$ did not
154 accumulate GFP in vacuoles in either CM or water and GFP-Atg8 accumulated in mycelial cytoplasm
155 under both conditions (**Fig. 4c**). These results indicated that $\Delta rim15$ strains were blocked in autophagy
156 and that, like in yeast¹⁹, *M. oryzae* Rim15 is required for autophagic flux but not for autophagy induction in
157 response to nutrient starvation.

158 GFP accumulated in vacuoles in *RIM15⁺* GFP-Atg8 IH during early biotrophic growth, at 28 hpi and 36
159 hpi, indicating autophagic activity was high in WT at these very early infection time points (**Fig. 4d,e**).
160 High autophagy activity in WT had not been shown before in *M. oryzae* IH and was unexpected at such
161 early timepoints. In contrast, in $\Delta rim15$ at 28 hpi and 36 hpi, GFP-Atg8 localized to the cytoplasm and did
162 not accumulate in vacuoles (**Fig. 4f,g**). Therefore, WT is undergoing autophagy during early biotrophic
163 infection, but autophagic flux was blocked in $\Delta rim15$. Note that 36 hpi corresponds in $\Delta rim15$ to mostly
164 intact biotrophic interfaces (**Fig. 1d**) and is on the cusp of the catastrophic interfacial membrane integrity
165 loss seen at 39 hpi and later for this mutant strain (**Fig. 2**).

166 **Rim15 is required for autophagic cycling *in planta***

167 Live-cell imaging at time points later than 36 hpi showed that GFP accumulated in $\Delta rim15$ vacuoles at 40
168 hpi and 44 hpi, suggesting that autophagic flux was delayed but not abolished in the mutant strain (**Fig.**
169 **5a**). GFP accumulated in *RIM15⁺* vacuoles at 44 hpi (**Fig. 5b**), indicating that autophagy is active as the
170 fungus is moving to neighbouring cells, which is consistent with our earlier findings that AM treatment
171 promotes cell-to-cell invasion¹³. However, we observed that autophagic flux was reduced in the *RIM15⁺*
172 GFP-Atg8 strain at 40 hpi, with most of the GFP signal accumulating as GFP-Atg8 in the cytoplasm (**Fig.**
173 **5b**). To understand autophagy dynamics better, we quantified the percentage of *M. oryzae* vacuoles

174 accumulating GFP, counted in fifty infected rice cells per time point (repeated in triplicate). This revealed
175 that in WT, autophagy activity levels cycle during biotrophic growth, but this autophagic cycling was
176 abolished in Δ rim15 (**Fig. 5c**). Thus, during biotrophy, Rim15 is required for autophagic cycling, a hitherto
177 unknown phenomenon in *M. oryzae* IH.

178 **Autophagic cycling is physiologically relevant to biotrophic colonization**

179 Previously, we had shown how treating WT-infected rice cells with the autophagy inhibitor 3-MA at 36 hpi
180 had, by 44 hpi, aborted IH growth and abolished cell-to-cell movement, thereby phenocopying the loss of
181 *IMP1*¹³. To determine if the autophagic cycling observed in **Fig. 5c** had physiological relevance during
182 infection, we treated WT-infected rice cells with 3-MA at 36, 40 and 44 hpi, corresponding to two peaks
183 and a trough of autophagy activity (**Fig. 5c**). When viewed at later time points, biotrophic growth was
184 attenuated in all cases following 3-MA treatment relative to the untreated WT control (**Supplementary**
185 **Fig. 2**). In many cases, a plant response was also visible (**Supplementary Fig. 2**). Therefore, blocking
186 autophagy during active autophagic cycling, including after IH has penetrated to the second infected rice
187 cell, aborted further IH growth, suggesting cycles of autophagy activity are required throughout biotrophy
188 for IH growth.

189 ***M. oryzae* Rim15 does not accumulate in the nucleus**

190 In yeast, under nutrient starvation and other stress conditions, Rim15 translocates to the host nucleus in a
191 manner dependent on cytoplasmic retention by Sch9^{21,26,27}. *M. oryzae* Rim15 carries predicted nuclear
192 localization signals (according to PSORTII), but even though the Δ rim15 *RIM15-GFP* complementation
193 strain expressed a functional Rim15-GFP protein (**Fig. 1b** and **Supplementary Fig. 3a**), Rim15-GFP only
194 localized to cytoplasm under both CM and nutrient-free axenic growth conditions (**Supplementary Fig.**
195 **3b**), and *in planta* at time points that corresponded with autophagic cycling and IH cell-to-cell movement
196 (shown for 36 hpi in **Supplementary Fig. 3c**). Expressing *RIM15-GFP* in a strain of *M. oryzae* carrying
197 histone H1 fused to RFP²⁸ confirmed no co-localization of Rim15-GFP with nuclei during biotrophy
198 (**Supplementary Fig. 3d**). Therefore, *M. oryzae* Rim15-GFP functions similarly to yeast Rim15, but
199 differences in ScRim15 and MoRim15 localization (at least under our tested conditions) may reflect
200 evolutionary changes in response to the different lifestyles of these two widely separated fungi.

201 **Rim15 is required for glutaminolysis**

202 To better understand the function of Rim15 in biotrophy, we turned our attention to *in planta* RNAseq data
203 obtained at 36 hpi (ie before Δ rim15 biotrophic interfacial membrane loss) from Δ rim15-, WT- and mock-
204 infected rice leaf sheaths (**Fig. 6a-e; Supplementary Tables 1-3**). GO and KEGG terms are consistent
205 with known Rim15 functions as well as our deduced *in planta* requirement for Rim15 in membrane
206 homeostasis (**Fig. 6d,e**). However, our attention was drawn to genes encoding enzymes of the GS-
207 GOGAT cycle²⁹ that were altered in expression in Δ rim15 IH at 36 hpi compared to WT (**Fig. 6f**). The GS-
208 GOGAT cycle is required for ammonium assimilation and glutamine homeostasis through the

209 interconversion of glutamine, glutamate and α -ketoglutarate. In addition, enzymes of the GS-GOGAT
210 cycle are also required for glutaminolysis, the use of glutamine or glutamate as carbon sources through
211 conversion to α -ketoglutarate. We focused on this pathway because we had plate test data in hand
212 showing that $\Delta rim15$ strains were attenuated for glutaminolysis (**Fig. 6g**). Specifically, $\Delta rim15$ growth was
213 severely restricted compared to WT on minimal media containing glutamine as the sole carbon and
214 nitrogen source, but $\Delta rim15$ grew more similar to WT on minimal media containing glucose as the
215 preferred carbon source and glutamine as the nitrogen source. Similar results were seen for growth on
216 glutamate compared to glucose + glutamate media.

217 The RNAseq and plate test data both pointed to GS-GOGAT cycle and glutaminolysis perturbations in
218 $\Delta rim15$. To better understand the connection between Rim15 and glutaminolysis, we extracted proteins
219 and metabolites for (phospho)proteomic and metabolomic analyses from WT and $\Delta rim15$ mycelia grown
220 in liquid minimal media with 0.5 mM glutamine as the sole carbon and nitrogen source. Proteomic
221 (**Supplementary Table 4**), quantitative phosphoproteomic (**Supplementary Table 5**) and metabolomic
222 (**Supplementary Table 6**) analyses on three independent mycelial samples per strain showed that, to a
223 greater or lesser extent, a number of proteins and metabolites associated with the GS-GOGAT pathway
224 and glutaminolysis were perturbed in $\Delta rim15$ compared to WT during growth under glutaminolytic
225 conditions (summarized in **Fig. 6h**). Most strikingly, $\Delta rim15$ perturbations to the GS-GOGAT cycle
226 resulted in a shift in glutamine/ glutamate homeostasis and a 2-fold decrease in α -ketoglutarate steady
227 state levels in $\Delta rim15$ vegetative hyphae compared to WT. Thus, glutaminolysis and the GS-GOGAT
228 cycle are perturbed in $\Delta rim15$, affecting α -ketoglutarate homeostasis.

229 **α -ketoglutarate treatment remedies $\Delta rim15$ biotrophic growth**

230 Based on the previous results, we hypothesized that Rim15-mediated glutaminolysis and the GS-GOGAT
231 cycle was required for biotrophy, and that the loss of α -ketoglutarate homeostasis in $\Delta rim15$ was
232 physiologically relevant to the infection process. We thus speculated that restoring α -ketoglutarate levels
233 in $\Delta rim15$ would improve infection. To test this, and before attempting to manipulate α -ketoglutarate levels
234 by pharmacological or genetic means, we first asked whether treating WT and $\Delta rim15$ -infected rice cells
235 with α -ketoglutarate affected biotrophic growth. **Fig. 7a** shows that treating $\Delta rim15$ -infected rice cells at
236 36 hpi with 10 mM α -ketoglutarate (as the cell-permeable dimethyl α -ketoglutarate (DMKG) analog)
237 completely remediated the $\Delta rim15$ mutant phenotype by 44 hpi. Compared to the untreated $\Delta rim15$
238 control, treatment with α -ketoglutarate promoted $\Delta rim15$ IH cell-to-cell movement and suppressed host
239 defense responses. $\Delta rim15$ IH in adjacent host cells were outlined with Bas4, indicating an intact EIHM,
240 and new BICs formed at IH tips. $\Delta rim15$ IH development and spread in α -ketoglutarate-treated rice leaf
241 sheaths was indistinguishable at 44 hpi from α -ketoglutarate-treated *RIM15⁺* IH, which was itself
242 indistinguishable from *RIM15⁺* IH growth and development in untreated rice cells (**Fig. 7a**). Using GFP-
243 Atg8 expressing strains, **Fig. 7b** shows that compared to the untreated $\Delta rim15$ control, α -ketoglutarate

244 treatment at 36 hpi suppressed $\Delta rim15$ autophagy by 44 hpi, leading to GFP-Atg8 accumulation in the
245 cytoplasm and little GFP accumulation in vacuoles. Similarly, α -ketoglutarate treatment of $RIM15^+$
246 infected cells at 36 hpi suppressed autophagy at 44 hpi, resulting in no GFP in vacuoles even though
247 $RIM15^+$ IH was extensively moving cell-to-cell by this time (**Fig. 7c**). This indicates that autophagy may
248 not be required for cell-to-cell spread in the presence of exogenous α -ketoglutarate. Together, our results
249 show that α -ketoglutarate treatment remediates $\Delta rim15$ biotrophic growth and suppresses autophagy *in*
250 *planta* in both $RIM15^+$ and $\Delta rim15$ IH.

251 **α -ketoglutarate signaling activates TOR and suppresses autophagic flux**

252 Next, because IH growth and autophagy suppression are indicative of TOR activity, we hypothesized that
253 α -ketoglutarate treatment activated TOR signaling. To test this notion, we studied the precise effect of α -
254 ketoglutarate treatment on autophagy and TOR activity by switching $RIM15^+$ GFP-ATG8 vegetative
255 mycelia from nutrient-rich liquid CM shaking cultures (where GFP-Atg8 was mostly in cytoplasm) into
256 water (where GFP accumulated in vacuoles) and into water + 10 mM α -ketoglutarate (as the cell-
257 permeable DMKG analog). Whereas switching vegetative hyphae into water alone triggered autophagy
258 (resulting in GFP accumulation in vacuoles), the addition of α -ketoglutarate was sufficient to suppress
259 autophagy (resulting in GFP-Atg8 accumulation in cytoplasm), even though other nutrients including a
260 nitrogen source were absent (**Fig. 7d**). Western blot analysis using anti-GFP antibody confirmed that α -
261 ketoglutarate treatment suppressed GFP-Atg8 processing to free GFP in water (**Fig. 7e**). Furthermore,
262 activated TOR phosphorylates Sch9 (the functional orthologue of p70 S6 kinase), and we previously
263 showed how Sch9 phospho-status in *M. oryzae* (and hence TOR kinase activity) can be probed using
264 anti-phospho-p70 S6 kinase antibody¹³. Western blots of proteins extracted from vegetative mycelia
265 revealed that, relative to growth in nutrient-rich CM, TOR kinase activity was reduced following growth in
266 water (as expected) but not in water treated with α -ketoglutarate (**Fig. 7f**). Together, our results show that
267 α -ketoglutarate activates TOR signaling and inhibits autophagy activity in the absence of other exogenous
268 nutrients. Furthermore, α -ketoglutarate is a carbon but not a nitrogen source and could not support fungal
269 growth alone. It can, however, be derived endogenously from the glutaminolysis of carbon- and nitrogen-
270 containing amino acids (a process perturbed in $\Delta rim15$). Therefore, we concluded from these experiments
271 that in WT, α -ketoglutarate is a metabolic signal, possibly a carbon and nitrogen sufficiency signal,
272 triggering TOR activation.

273 **Treatment with glutamine and glutamate, but not ammonium or asparagine, remediates $\Delta rim15$
274 biotrophic growth in a dose-dependent manner**

275 We next tested whether other glutaminolysis-related metabolites remediated $\Delta rim15$ biotrophic growth.
276 Following treatment at 36 hpi, we found that by 44 hpi, cell-to-cell spread of $\Delta rim15$ IH was remediated by
277 10 mM glutamine and 10 mM glutamate treatment, but not by 10 mM ammonium (NH_4^+) treatment
278 (**Supplementary Fig. 4**). Treatment with 10 mM asparagine, which is not a glutaminolytic intermediate

279 nor part of the GS-GOGAT cycle, also did not remediate $\Delta rim15$ biotrophic growth (**Supplementary Fig.**
280 **4**). Furthermore, remediation by glutamine was dose-dependent, such that ≤ 1 mM exogenous glutamine
281 did not remediate $\Delta rim15$ IH growth (**Supplementary Fig. 5**). In $RIM15^+$ IH, treatment with glutamine,
282 glutamate or asparagine at 36 hpi had no effect on growth by 44 hpi, but NH_4^+ treatment partially inhibited
283 $RIM15^+$ IH growth in the second infected rice cells and also led to partial loss of $RIM15^+$ biotrophic
284 membranes (**Supplementary Fig. 4**). Together (and when considered along with the GS-GOGAT results
285 below), our interpretation is that exogenous treatments with 10 mM glutamine or 10 mM glutamate drive
286 α -ketoglutarate production, resulting in remediation of $\Delta rim15$ IH biotrophic growth. Furthermore, our
287 results indicate that the acquisition of these amino acids from the host plant cell by $\Delta rim15$ must be
288 extremely limited (or else $\Delta rim15$ IH growth would not be impaired), consistent with previous genetic-
289 based observations of, amongst others, the $\Delta asn1$ asparagine auxotroph¹⁶. We can here for the first time
290 extend this principle to WT because 10 mM α -ketoglutarate treatment suppressed WT autophagy at 44
291 hpi (**Fig. 7c**), suggesting α -ketoglutarate-generating host nutrients are inaccessible to WT during
292 biotrophy, at least in concentrations required to suppress autophagy.

293 **Glutamine treatment remediates $\Delta imp1$ biotrophic growth**

294 Live-cell imaging showed that 10 mM glutamine treatment of detached rice leaf sheaths at 36 hpi also
295 remediated $\Delta imp1$ biotrophic growth by 44 hpi (**Supplementary Fig. 6**). Glutamine was applied here
296 rather than α -ketoglutarate (as cell-permeable DMKG) in order to determine if $\Delta imp1$ IH could actively
297 transport amino acids into cells. Because exogenous glutamine treatment remediated $\Delta imp1$ IH growth
298 and cell-to-cell spread, this provides evidence that, like for $\Delta rim15$, $\Delta imp1$ cannot access sufficient
299 quantities of host glutamine to promote biotrophic growth. These results also point to Imp1 and thus
300 autophagy acting upstream of the α -ketoglutarate signal.

301 **The GS-GOGAT cycle is required for α -ketoglutarate signaling**

302 Pharmacological evidence that the GS-GOGAT cycle is required for biotrophic growth and interfacial
303 membrane integrity is shown in **Fig. 8**. Treatment of WT-infected detached rice leaf sheaths at 36 hpi with
304 the irreversible glutamine synthetase (GS) inhibitor methionine sulfoximine (MSO), or with the GOGAT
305 inhibitor azaserine (AZS), had, in both cases by 44 hpi, resulted in attenuated growth and the loss of the
306 EIHM, resulting in Bas4 in the rice cytoplasm. Unlike in $\Delta rim15$ -infected rice cells, MSO- and AZS-treated
307 WT-infected rice cells retained a small BIC, although in both cases Pwl2 had leaked into the rice
308 cytoplasm, which was clearly seen in the red channel in **Fig. 8**, indicating BIC integrity was compromised
309 compared to the untreated control. AZS-induced attenuation of IH growth and biotrophic interfacial
310 membrane integrity was remediated by addition of the GOGAT product glutamate, while MSO toxicity was
311 remediated by addition of the GS product glutamine, thus confirming AZS and MSO, respectively, as
312 specific fungal GS-GOGAT cycle inhibitors *in planta*. Importantly, α -ketoglutarate treatment remediated
313 MSO- and AZS-induced biotrophic growth defects. Together, these results directly implicate the GS-

314 GOGAT cycle in biotrophic growth and interfacial membrane integrity as a means to supply α -
315 ketoglutarate for downstream signaling purposes. These results also demonstrate how α -ketoglutarate,
316 and not its conversion to glutamine or glutamate, is the TOR activating signal.

317 **Autophagy-dependent biotrophic growth and interfacial membrane integrity requires amino acid
318 prototrophy upstream of the α -ketoglutarate signal**

319 We next found that IH growth and biotrophic interfacial membrane integrity was dependent on *M. oryzae*
320 amino acid prototrophy upstream of α -ketoglutarate signaling. In a previous study, we showed that an *M.*
321 *oryzae* asparagine auxotroph lacking asparagine synthetase, $\Delta\text{asn}1$, made functional appressoria and
322 elaborated IH but failed to establish extensive biotrophic growth in the first infected rice cell, indicating
323 asparagine and perhaps other amino acids were not accessible to this mutant strain during biotrophy¹⁶.
324 Here, we asked, what happens to $\Delta\text{asn}1$ biotrophic interfaces when IH growth is aborted, and can $\Delta\text{asn}1$
325 IH growth be remediated by α -ketoglutarate? To address these questions, we knocked out *ASN1* in our
326 strain carrying pBV591 to generate the mutant strain $\Delta\text{asn}1\text{ PWL2-mCherry}^{\text{NLS}}\text{ Bas4-GFP}$. Live-cell
327 imaging showed that by 44 hpi, this mutant strain had lost EIHM integrity, as evidenced by Bas4 in the
328 rice cytoplasm, suggesting autophagy was impaired (**Fig. 9a**). The $\Delta\text{asn}1$ BIC was disrupted at 44 hpi
329 but not entirely eradicated, although Pwl2 was observed in the rice cytoplasm, suggesting $\Delta\text{asn}1$ BIC
330 integrity was compromised and leaking Pwl2 (**Fig. 9a**). $\Delta\text{asn}1$ IH growth was partially restored (ie $\Delta\text{asn}1$
331 IH did not fill the first infected cell), and cell-to-cell movement and biotrophic membrane integrity was fully
332 restored, following treatment of infected rice leaf sheaths with 10 mM asparagine at 36 hpi (**Fig. 9b**). Note
333 that in an earlier report¹⁶, 10 mM asparagine added at 0 hpi to spore suspensions did not remediate
334 biotrophic growth, indicating that the timing and means of application of remediating treatments for IH
335 growth mutants is critical. Like for Δrim15 , treatment with α -ketoglutarate remediated $\Delta\text{asn}1$ biotrophic
336 interfacial membrane integrity and cell-to-cell movement, although this occurred without filling the first
337 infected rice cell, suggesting α -ketoglutarate triggered IH growth but sustained IH growth was not fully
338 supported by the loss of *de novo* asparagine biosynthesis (**Fig. 9b**). However, unlike for Δrim15 (and
339 Δimp1), $\Delta\text{asn}1$ IH growth and biotrophic interfacial membrane integrity was not remediated by treatment
340 with the TOR-independent autophagy inducer AM (**Fig. 9b**). Thus, amino acid prototrophy is required for
341 autophagy-mediated (but not α -ketoglutarate-mediated) biotrophic growth and interfacial membrane
342 integrity. This suggests that α -ketoglutarate signaling is downstream of amino acid prototrophy-dependent
343 autophagy.

344 **α -ketoglutarate remediates IH growth following autophagy blocking by 3-MA**

345 Although α -ketoglutarate activates TOR and suppresses autophagy, when considering that autophagy in
346 IH is cyclical, that Imp1 and thus autophagy is upstream of α -ketoglutarate signaling, and that α -
347 ketoglutarate treatment remediated IH growth following the loss of amino acid prototrophy-dependent

348 autophagy, we hypothesized that α -ketoglutarate was an autophagy-derived growth signaling metabolite.
349 To test this, we asked whether α -ketoglutarate treatment could remediate IH growth following autophagy
350 blocking by 3-MA. **Fig. 10a** shows that it can. WT-infected rice cells were treated with 3-MA at 36 hpi.
351 Compared to the replacement of this treatment with water at 40 hpi, replacing 3-MA at 40 hpi with α -
352 ketoglutarate (as DMKG) resulted, by 44 hpi, in IH growth, biotrophic membrane integrity and the
353 suppression of host plant defense responses (**Fig. 10a**). Thus, α -ketoglutarate treatment by-passes the 3-
354 MA-mediated autophagy block that otherwise results in the loss of membrane integrity and aborted
355 biotrophy. We conclude that α -ketoglutarate is an autophagy-derived, TOR-activating signaling molecule.

356 Discussion

357 Many important eukaryotic filamentous plant pathogens exhibit a symptomless biotrophic growth stage,
358 where microbial cells grow in living host plant cells separated from host cytoplasm by extensive biotrophic
359 interfaces, but little is known about the molecular and metabolic drivers involved. The major findings of
360 this work help to fill these knowledge gaps. By showing how fungal metabolism is integrated with
361 biotrophic growth, interfacial membrane integrity and host defense suppression during growth in living
362 host rice cells, we shed considerable new light on understanding how the cells of one organism can grow
363 in the cells of another.

364 Following an initial period of IH elaboration and biotrophic interface construction, which does not require
365 *RIM15* but (at least for early IH growth) does require glucose-mediated TOR activation³⁰, all our data
366 together fit the model in **Fig. 10b**. This shows how α -ketoglutarate liberated by *M. oryzae* autophagy,
367 which is cyclical during biotrophic growth in host rice cells, reactivates TOR to stimulate extensive
368 biotrophic growth and maintain interfacial membrane integrity under the nutrient-restricted
369 microenvironment of the host rice cell. More specifically, because α -ketoglutarate is generated in cells
370 from amino acids via glutaminolysis and the GS-GOGAT cycle – processes shown here to be essential
371 for biotrophic growth – we propose that α -ketoglutarate is a TOR-triggering amino acid-sufficiency signal.
372 Consequently, as excess amino acids are consumed for growth, α -ketoglutarate is depleted, TOR is
373 inactivated and autophagy is induced again. Discovering that autophagy mediates intracellular pathogen
374 growth through the supply of α -ketoglutarate is significant because although the function of autophagy in
375 cells is well understood, few physiological roles – including how autophagy-derived metabolites are used
376 by cells – are known³¹.

377 Uncovering pivotal roles for autophagy and α -ketoglutarate in pathogenicity could lead to the
378 development of disease management strategies applicable to a wide range of pathosystems with similar
379 infection strategies. These findings may also improve our understanding of the metabolic underpinnings
380 of intracellular pathogens more generally. However, because our treatment data provide the most
381 compelling evidence to date that host nutrient acquisition by *M. oryzae* is very low or possibly, at least for

382 some metabolites, non-existent (perhaps as a means to avoid detection by the host plant), caution must
383 be taken when considering mitigation strategies based around limiting fungal access to host nutrients.

384 The TOR-activating role deduced here for α -ketoglutarate, which occurs even in the absence of a
385 nitrogen source, has not been previously described for any plant pathogen, but our findings are inline with
386 studies showing how α -ketoglutarate production from glutaminolysis, and treatment with the cell-permeable
387 α -ketoglutarate analogue, stimulated mTORC1 activation in human cells³². Moreover, supplementation
388 with glutamine alone was sufficient to restore mTORC1 activity in mouse embryonic fibroblasts (MEFs)
389 following a prolonged period of amino acid starvation, and mTORC1 reactivation after starvation in MEFs
390 was autophagy-dependent³³. Thus, the general principles of α -ketoglutarate-mediated TOR reactivation
391 we describe, essential for regulating cell growth under nutrient-limited conditions, might be widespread.

392 In general, the multiomics data are consistent with both the Rim15 functions described in yeast and the
393 *M. oryzae* Δ rim15 phenotype elaborated here. For example, loss of *R/M15* affects processes related to
394 membrane biogenesis, nitrogen metabolism and sugar metabolism *in planta*. Thus, answers to
395 outstanding questions about Rim15 function may be found in our genome-wide data sets. For example,
396 how does Rim15 regulate autophagy and glutaminolysis? A protein encoded by a GCN4 homologue
397 (MGG_00602) was decreased 4.5 fold in phosphorylation levels in Δ rim15 compared to WT under
398 glutaminolytic growth conditions (**Supplementary Table 5**). Yeast Gcn4 is a transcriptional activator of
399 amino acid biosynthetic genes under amino acid starvation conditions, including genes of the GS-GOGAT
400 pathway, and it is also required for nitrogen- and amino acid starvation-induced autophagy gene
401 expression^{20,34-38}. Conceivably, control of autophagy and glutaminolysis might occur, directly or indirectly,
402 via a MoRim15-MoGcn4 signaling axis. Another question to consider is why did Δ rim15-infected rice cells
403 accumulate ROS and trigger stronger host defenses than Δ imp1? Glutathione levels were reduced in
404 Δ rim15 (**Supplementary Table 7**), possibly due to perturbed glutamate allocation through the GS-GOGAT
405 cycle, while the protein encoded at MGG_02408, a homologue of the yeast transcriptional activator of
406 stress response genes Asg1, was 100-fold reduced in phosphorylation levels in Δ rim15 vegetative
407 mycelia compared to WT (**Supplementary Table 5**), together suggesting how Rim15 might contribute to
408 redox balance and ROS scavenging *in planta*. Finally, a putative glutamate symporter, MGG_07639,
409 annotated at NCBI as encoding a homologue of excitatory amino acid transporter 2 (EAAT2), is
410 downregulated 10-fold in Δ rim15-infected rice cells at 36 hpi compared to WT (**Supplementary Table 1**),
411 indicating how at least some selective host nutrient acquisition might occur *in planta* in a Rim15-
412 dependent manner.

413 To conclude, this work provides an unparalleled description of the core metabolic strategies required for
414 establishing fungal biotrophic growth in host plant cells, and points to Rim15-mediated networks of gene,
415 protein and metabolic interactions underlying infection. As the climate changes, the number and
416 assemblages of eukaryotic filamentous plant pathogens pressuring food security will change and new

417 threats will emerge³⁹. Combatting these threats in a robust and sustainable manner will require a more
418 detailed and comprehensive understanding of the molecular factors facilitating pathogen invasion of host
419 plant cells. By deducing how α -ketoglutarate – revealed here as a key integrator of carbon and nitrogen
420 metabolism – connects autophagic cycling and TOR signaling to support pathogen growth and metabolic
421 homeostasis in the absence of extensive nutrient acquisition from the host, we provide a solid foundation
422 for future studies probing and interpreting fungal metabolism in host cells. Such studies might foster the
423 discovery of new and targetable pathogen weaknesses with broad applicability.

424 Materials and methods

425 Fungal strains and growth conditions

426 The *M. oryzae* Guy11 rice isolate was used as the wild type (WT) strain for this study². Strains used in
427 this study are listed in **Supplementary Table 8** and are maintained as filter stocks in the Wilson lab.
428 Strains were grown at 26 °C on solid and liquid CM or minimal media as described in detail previously^{13,40}.
429 *In vitro* fungal physiological analyses were performed as described previously¹³, and specific details are
430 provided in the text.

431 Plant inoculations and live-cell imaging

432 For whole plant inoculations, spores of the indicated strains were harvested from colonies grown on solid
433 oatmeal agar plates for 14 days and applied to 3-week-old rice seedlings of the susceptible cultivar CO-
434 39 at a rate of 1×10^5 spores ml⁻¹. Images were recorded at 5 days post inoculation. For live-cell imaging,
435 spores of the indicated strains were harvested from 14-day-old colonies grown on solid oatmeal agar
436 plates and inoculated at a rate of 2×10^4 spores ml⁻¹ onto detached rice leaf sheaths from 4-week-old rice
437 seedlings of the susceptible cultivar CO-39, as described previously¹³. Leaf sheath cells were imaged at
438 the indicated times using a Nikon Eclipse Ni-E upright microscope and NIS Elements software. Unless
439 otherwise specified, treatments were added at 36 hpi and viewed at 44 hpi. Treatments were added at the
440 concentrations indicated. Treatments were purchased from Sigma-Aldrich, USA. Cells were stained with 1
441 mg ml⁻¹ 3,3'-diaminobenzidine (DAB, Sigma-Aldrich) as previously described⁹. All treatment assays were
442 performed at least in triplicate and representative images are shown.

443 Detached rice leaf sheath assays and artificial hydrophobic surfaces were used to quantify appressorium
444 formation rates. Appressorium penetration rates and rates of IH cell-to-cell movement to adjacent cells
445 were determined using detached rice leaf sheaths. Appressorial formation rates were determined by
446 examining how many of 50 spores had formed appressoria by 24 hpi on artificial hydrophobic surfaces
447 (after applying at a rate of 1×10^4 spores ml⁻¹) or on rice leaf sheath surfaces, repeated in triplicate.
448 Penetration rates were determined by examining how many of 50 appressoria on one rice leaf sheath
449 surface had penetrated into underlying cells by 30 hpi, repeated in triplicate. Rates of cell-to-cell
450 movement were determined by observing how many of 50 primary infected rice cells had formed IH in
451 adjacent cells by 48 hpi, repeated in triplicate.

452 **Generation of targeted gene deletion mutant strains in *M. oryzae***

453 Genes were disrupted in *M. oryzae* using the split marker technique¹³ and the primers are listed in
454 **Supplementary Table 9**. *RIM15* and *ASN1* genes were replaced with the *ILV2* gene conferring
455 resistance to sulphonyl urea. Transformants were confirmed by PCR. At least two independent deletants
456 per gene knockout were characterized fully and shown to be indistinguishable.

457 **Generation of strains producing fluorescently labelled proteins**

458 *M. oryzae* gene sequences obtained from the *M. oryzae* genome database
459 (http://fungi.ensembl.org/Magnaporthe_oryzae/Info/Index) were used to design the primers in
460 **Supplementary Table 9** that were then used for constructing the vectors in **Supplementary Table 10**.
461 The full length CDS of *ATG8* was amplified from Guy11 with RP27-NGFP-ATG8-F /-R primers. The end
462 of the PCR product contained 15~20 bases homologous to the pGTN vector. The purified PCR product
463 was fused with linearized pGTN, which was digested with NotI using the In-Fusion HD enzyme kit. The
464 reaction mixture was transferred into the *E. coli* DH5a strain with ampicillin antibiotic screening, and all
465 colonies were identified by PCR and plasmid integrity was verified by sequencing. The vector was then
466 transformed into WT and $\Delta rim15$ protoplasts, respectively. All *M. oryzae* transformants were screened for
467 geneticin resistance and confirmed by PCR. Five independent transformants per parental strain were
468 characterized and found to have identical phenotypes. A similar procedure was used to construct the
469 *RIM15-GFP* vector, except pGTN was linearized with HindIII and BamHI to insert *RIM15* upstream of
470 *GFP*. To generate $\Delta rim15$ strains producing Pwl2-mCherry^{NLS} and Bas4-GFP, the $\Delta rim15$ parental strain
471 was transformed with the pBV591 vector⁶ and selected using hygromycin resistance. Three independent
472 transformants were fully characterized and found to have identical phenotypes. To generate $\Delta asn1$
473 strains producing Pwl2-mCherry^{NLS} and Bas4-GFP, *ASN1* was disrupted in our *ASN1*⁺ strain carrying
474 pBV591. Following transformation, at least 5 independent mutant strains were screened for fluorescence
475 in rice leaf sheath assays.

476 **RNA extraction and RNAseq analysis**

477 4-week-old rice detached rice leaf sheaths were inoculated with spores of the WT and $\Delta rim15$ mutant
478 strain at a rate of 1×10^5 spores mL⁻¹. Detached rice leaf sheaths inoculated with mock solution (0.2%
479 gelatin) was used as the control. At 36 hpi, the inoculated leaf sheaths were harvested and flash frozen in
480 liquid nitrogen. Three biological replicates of each treatment were used for the following RNA sequencing
481 analysis. For RNA extraction, leaf sheath tissues were ground in liquid nitrogen, and total RNA was
482 extracted using the TRIzol reagent (Invitrogen, US), according to the manufacturer's standard procedure.
483 Following removal of contaminating genomic DNA using DNase I, total RNA was purified with PureLink
484 RNA Mini kit (Thermo Fisher Scientific, US) by following the manufacture's instruction manual. Total RNA
485 quality was estimated by running on a denatured agarose gel, and the RNA quantity was measured using
486 a Nanodrop Spectrophotometer. RNA integrity and purity were evaluated using the Agilent Technologies

487 2100 Bioanalyzer, and high quality (RIN \geq 7.0) was confirmed for all samples. For each sample, 3 μ g of
488 total RNA at a concentration of more than 100 ng/ μ l was used in library construction.

489 For library construction and sequencing, Poly(A) RNA sequencing library was prepared following
490 Illumina's TruSeq-stranded-mRNA sample preparation protocol. Poly(A) tail-containing mRNAs were
491 isolated from total RNA using oligo-(dT) magnetic beads with two rounds of purification. Then, the poly(A)
492 mRNA fractions were cleaved into smaller fragments using divalent cation buffer in elevated temperature.
493 The cleaved RNA fragments were reverse-transcribed to create the final cDNA library in accordance with
494 a strand-specific library preparation by dUTP method. Quality control analysis and quantification of the
495 sequencing library were performed using Agilent Technologies 2100 Bioanalyzer High Sensitivity DNA
496 Chip. The average insert size for the paired-end libraries was 300 ± 50 bp. Sequencing of generated
497 cDNA libraries was performed with 150-nucleotide pair-end reads on Illumina's NovaSeq 6000
498 sequencing system at LC Sciences (US) following the vendor's recommended protocol. Three biological
499 replications were used for RNA-seq experiments.

500 For transcriptomic analysis of differentially expressed genes, with reads mapping to the reference
501 genome, raw sequencing data were first filtered by removing contaminated adaptor sequences, low
502 quality bases and undetermined bases using CUTADAPT⁴¹ and perl scripts in LC Science. Then,
503 sequence quality was verified using FastQC (<http://www.bioinformatics.babraham.ac.uk/projects/fastqc/>).
504 Following removal of 9 bp of low quality bases from the 5'-ends of the reads using SEQTK (version 1.2)
505 (<https://github.com/lh3/seqtk>), valid reads in high quality were mapped to the *Magnaporthe oryzae*
506 genome assembly (https://ftp.ncbi.nlm.nih.gov/genomes/all/GCF/000/002/495/GCF_000002495.2_MG8/)
507 using SUBREAD for Unix (version 2.0)⁴². The alignment was carried out for read groups of all samples,
508 including all replications of wild type Guy11, *Δrim15*, and mock control. Gene annotation as GTF (version
509 2.2) was obtained from NCBI, corresponding to the MG8 genome assembly GCF_000002495.2. Read
510 counts per-gene were computed using FEATURECOUNTS⁴³ from SUBREAD (version 2.0). After
511 removing genes with the counts per million (CPM) less than one in two samples, the count data of the
512 remaining genes were subjected to the Relative Log Expression normalization and then used in the
513 identification of differentially expressed genes using DESEQ2 (version 1.14.0)⁴⁴ in R by comparing the
514 expression of genes in samples inoculated with the *Δrim15* mutant, Guy11, or mock control, with
515 differentially expressed genes defined as having adjusted *P* value < 0.05 and absolute log₂ of fold change
516 between test and control value of ≥ 1 . Genes that were defined as non-differentially expressed were those
517 having adjusted *P* value ≥ 0.05 or absolute log₂ of fold change between test and control value of < 1 . All
518 counts data and DESeq2 analysis results are listed in the **Supplementary Table 1**. Moreover, for all
519 genes in this table, functional and pathway annotations were conducted and achieved by active data
520 mining through interactively calling the BioMart (<http://www.biomart.org/>, version 0.7), GO
521 (<http://geneontology.org/>, Release 2022-01-13), and KEGG (<https://www.genome.jp/kegg/>, Release
522 101.0, January 1, 2022) databases and by subsequent integration in R (version 4.1.2).

523 To evaluate the quality consistency of samples, Principal Component Analysis (PCA) was performed
524 using DESeq2 pipeline with the count matrix calculated by the variance stabilizing transformation (VST)
525 used as the input.

526 To visualize the DEGs, a Volcano Plot was generated using ggplot2 (version 3.3.5)⁴⁵ in R.

527 To identify genes with similar expression patterns, following the rlog transformation of the count matrix,
528 bidirectional hierarchical clustering⁴⁶ based on Euclidean distance⁴⁷ was performed for the top 100 DEGs
529 using the pheatmap package (version 1.0.2, [https://cran.r-
530 project.org/web/packages/pheatmap/index.html](https://cran.r-project.org/web/packages/pheatmap/index.html))⁴⁸ in R.

531 Gene Ontology (GO)⁴⁹ enrichment analysis and Kyoto Encyclopedia of Genes and Genomes (KEGG)⁵⁰
532 pathway enrichment analysis for the DEGs were conducted using DAVID 2021(released Dec, 2021)^{51,52}.
533 The identified GO ontologies are listed in the **Supplementary Table 2**. The identified KEGG pathways
534 are listed in **Supplementary Table 3**.

535 All plots generated from bioinformatics analysis were plotted in R (version 4.1.2). All bioinformatics
536 analyses following the adaptor removal were performed utilizing the High Performance Computing
537 Resources at the Holland Computing Center, University of Nebraska-Lincoln, USA.

538 **Protein extraction, proteomics and phosphoprotein enrichment**

539 Strains were grown as mycelia in liquid CM for 42 hr before shifting to minimal media with 0.5 mM
540 glutamine as the sole carbon and nitrogen source for 16 hr.

541 For the proteomics experiments, 0.3g of wet mycelia per strain (in triplicate) was lysed in 1 mL lysis buffer
542 consisting of 7M urea, 2M thiourea, 5 mM DTT, 100mM tris/HCl pH 7.8, and containing 1X complete
543 EDTA-free protease inhibitor and 1X PhosStop phosphatase inhibitor, for 10 min at 20 Hz on a
544 mechanical tissue lyser. Protein was precipitated with acetone and the pellet was washed and
545 redissolved in the lysis buffer containing 2X PhosStop phosphatase inhibitor. The proteins were assayed
546 using the CBX kit (G-Bioscience). An aliquot of proteins was reduced with DTT and alkylated with
547 iodoacetamide prior to digestion with LysC and then trypsin. Each digest was analyzed by nanoLC-
548 MS/MS using a 2h gradient on a Waters CSH 0.075 mm x 250 mm C18 column feeding into an Orbitrap
549 Eclipse mass spectrometer. However, an unknown component interfered with the chromatography and
550 samples were rerun after offline solid-phase C18 clean-up (Waters SepPak, 100mg 1cc syringe
551 cartridges).

552 For phosphoprotein enrichment, of the 1mg of wet mycelia from each strain (in triplicate), 0.95mg was
553 used for TiO2 phosphopeptide enrichment with lactic acid. Samples were subjected to offline solid-phase
554 C18 clean-up (Waters SepPak, 100 mg 1cc syringe cartridges). Each cleaned sample was then analyzed
555 by nanoLC-MS/MS using a 2 h gradient on a Waters CSH 0.075 mm x 2 50 mm C18 column feeding into
556 an Orbitrap Eclipse mass spectrometer.

557 Quantification of the proteins and phosphoproteins was performed separately using Proteome Discoverer
558 (Thermo; version 2.4). All MS/MS samples were searched using Mascot (Matrix Science, London, UK;
559 version 2.6.2). Mascot was set up to search the cRAP_20150130.fasta (124 entries); uniprot-
560 refprot_UP000009058_Magnaporthe_oryzae 20210511 (12,791 sequences); assuming the digestion
561 enzyme trypsin. Mascot was searched with a fragment ion mass tolerance of 0.06 Da and a parent ion
562 tolerance of 10.0 PPM. For the proteomics experiment, deamidation of asparagine and glutamine and
563 oxidation of methionine were specified in Mascot as variable modifications while carbamidomethyl of
564 cysteine was specified as fixed modification. For the phosphoproteomics experiment, deamidation of
565 asparagine and glutamine, oxidation of methionine, phosphorylation of serine, threonine and tyrosine, and
566 acetylation of N-term were specified in Mascot as variable modifications while carbamidomethyl of
567 cysteine was specified as fixed modification. Peptides were validated by Percolator with a 0.01 posterior
568 error probability (PEP) threshold. The data were searched using a decoy database to set the false
569 discovery rate to 1% (high confidence). Only proteins with a minimum of 2 peptides and 5 PSMs were
570 reported. For phosphopeptides, the minimum was 1 phosphopeptide and 3 PSMs. The localization
571 probability of the phosphorylation sites is calculated using PtMS⁵³. Probabilities are indicated in
572 parenthesis next to the amino acid residue. If there is no probability indicated, this means that the
573 phosphorylation of the peptide was not confidently localized.

574 The peptides and phosphopeptides were quantified using the precursor abundance based on intensity.
575 Normalized and scaled abundances are reported. The peak abundance was normalized using total
576 peptide amount. The peptide group abundances are summed for each sample and the maximum sum for
577 all files is determined. The normalization factor used is the factor of the sum of the sample and the
578 maximum sum in all files. Then, abundances were scaled so that the average of the abundances is equal
579 to 100 for each sample. The imputation mode was used to fill the gaps from missing values. The protein
580 and phosphoprotein ratios are calculated using summed abundance for each replicate separately and the
581 geometric median of the resulting ratios is used as the protein ratios. The significance of differential
582 expression is tested using a t-test which provides a p-value and an adjusted p-value using the Benjamini-
583 Hochberg method for all the calculated ratios.

584 **Metabolite extraction and metabolomics**

585 Strains were grown as mycelia in liquid CM for 42 hr before shifting to minimal media with 0.5 mM
586 glutamine as the sole carbon and nitrogen source for 16 hr. Samples were lyophilized before metabolite
587 extraction.

588 For the metabolomic results in **Supplementary Table 6**, an aliquot of 20-25 mg of each sample was
589 extracted for polar compounds using the chloroform/methanol/water extraction (Folch Method). The
590 extracts were dried down and derivatized for GCMS using MSTFA+TMCS. The samples were run
591 alongside the mixture of retention index C10-25 alkanes for identification. The data was analyzed using
592 MS-Dial (<https://doi.org/10.1038/nmeth.3393>) for peak detection, deconvolution, alignment, quantification

593 and identification. The library used was the curated Kovats RI (28,220 compounds, which includes the
594 Fiehn, RIKEN and MoNA databases). The peaks were reviewed and the final list of compounds with RI
595 similarities >90% were reported. Highlighted in red in **Supplementary Table 6** are compounds with ID
596 confirmed by authentic standards or by complementary search of the NIST14 library using NIST-MS. The
597 peak area was normalized based on the total ion chromatogram for the assigned metabolites using sum
598 normalization in MetaboAnalyst 5.0.

599 For the metabolomic results in **Supplementary Table 7**, the samples were suspended in 500 uL of
600 extraction solution on dry ice, and disrupted by 4 cycles of the bullet blender at a setting of “7” for 3
601 minutes each. The suspension was centrifuged for 10 min at 15,000 xg. The supernatant was transferred
602 into a second tube and evaporated using a speed Vac at 4 °C. The pellet was resuspended into 100 uL of
603 LC-Grade water and transferred into V-vials and placed in the autosampler. The sample concentrations
604 are reported in micromolar units, and the metabolite levels were normalized by weight.

605 **Western blot analysis**

606 For S6K phospho-status analysis, indicated strains were inoculated in liquid CM medium and shaking
607 cultured for 42 hr. After being excessively washed with H₂O, the vegetative hyphae were aliquoted into
608 liquid CM, H₂O, and H₂O containing 10 mM DMKG (Dimethyl 2-oxoglutarate, a permeable version of a-
609 ketoglutarate), respectively. Following 4 hr of further shaking culture, the vegetative hyphae were
610 harvested and frozen in liquid nitrogen. For immunoblotting analysis, equal amounts of pulverized mycelia
611 were resuspended in denaturing lysis buffer (62.5 mM Tris HCl, pH 6.8, 3% SDS, 10% glycerol, 5% 2-
612 mercaptoethanol) supplemented with protease inhibitors (200 mM AEBSF, 20 mM Bestatin, 5mM E-64,
613 10 mM Leupeptin, 10 mM Pepstatin A, 500 mM 1,10-Phenanthroline, 5 mM EDTA, 1 mM PMSF) and
614 phosphatase inhibitors (20 mM NaF, 0.2 M okadaic acid, 20 mM b-glycerophosphate, 5mM Na₃VO₄),
615 followed by denaturation at 95°C for 5 min. After clearing the cell lysates by centrifugation at 16,000 g for
616 15 min at 4°C, equal volume of the lysate per sample were resolved in a 12% (wt/vol, polyacrylamide)
617 SDS-PAGE gel and blotted onto an Immun-Blot PVDF membrane (Bio-Rad, USA). For phospho-p70 S6
618 kinase detection, the membrane was first incubated in the blocking buffer (5% BSA in 1xTBS) for 12
619 hours at 4°C, and then incubated with anti-phospho-p70 S6 kinase α antibody (monoclonal, produced in
620 mouse, Santa Cruz Biotechnology, USA; 1:500 dilution) in 1xTBS containing 1% BSA for 16 hours at 4°C.
621 After being washed in 1xTBST for three times with 5 min each, the membrane was incubated with anti-
622 mouse IgG-peroxidase (produced in goat, Sigma, USA; 1:10,000 dilution) in 1xTBST containing 1% BSA
623 for 12 hours at 4°C. After being washed in 1xTBST for three times with 5 min each, the blot was imaged
624 using Clarity Western ECL chemiluminescent system (Bio-Rad). Following stripping the anti-phospho-p70
625 S6 kinase α antibody off the membrane, as a loading reference, α-tubulin was visualized using anti-
626 Tub(α) antibody (monoclonal, produced in rat, Santa Cruz Biotechnology, USA; 1:1,000 dilution) in 1xTBS
627 containing 5% non-fat milk for 1 hour at room temperature, followed by probing with anti-rat IgG-
628 peroxidase (produced in goat, Santa Cruz Biotechnology, USA; 1:10,000 dilution) in 1xTBST containing

629 5% non-fat milk for 1 hour at room temperature. The imaged blots were quantitated by densitometry using
630 ImageJ analysis software (imagej.net/Welcome). Relative signal intensity of the phospho-p70 S6 Kinase
631 was obtained by normalizing against α -tubulin and then by correcting for the background determined from
632 a WT control strain. To eliminate protein degradation and protein dephosphorylation, low temperature
633 (4°C), protease inhibitors and phosphatase inhibitors were applied throughout the western blot analysis,
634 including protein transfer, membrane blocking, and antibody binding steps.

635 In addition, to monitor the presence of autophagy in each sample, the intact GFP-Atg8 and the cleaved
636 free GFP were visualized using Anti-Green Fluorescent Protein (GFP) antibody (monoclonal, produced in
637 mouse, Sigma, USA; 1:1,000 dilution) in 1xTBS containing 5% non-fat milk for 2 hours at room
638 temperature, followed by probing with anti-mouse IgG-peroxidase (produced in goat, Sigma, USA;
639 1:10,000 dilution) in 1xTBST containing 5% non-fat milk for 1 hour at room temperature. As a loading
640 reference, α -tubulin in all samples was visualized using anti-Tub(α) antibody following stripping the Anti-
641 Green Fluorescent Protein (GFP) antibody off the membrane.

642 Acknowledgements

643 This work was supported by National Science Foundation funding (IOS-1758805) to RAW. ZG was
644 supported by funding from the China Scholarship Council. We thank Dr. Sophie Alvarez of the Center for
645 Biotechnology, University of Nebraska-Lincoln, for the (phospho)proteomic and metabolomic analyses in
646 Supplementary Tables 4-6. We thank Dr. Javier Seravalli of the Redox Biology Center, University of
647 Nebraska-Lincoln, for the metabolomic analysis in Supplementary Table 7. Bioinformatic analyses were
648 completed using the supercomputing resources of the Holland Computing Center at the University of
649 Nebraska-Lincoln, which receives support from the Nebraska Research Initiative.

650 Author contributions

651 RAW conceived the project and obtained funding. GL and RAW designed the experiments and
652 interpreted the data. GL, ZG, ND and ROR performed the experiments. Specifically, GL generated and
653 characterized the Δ rim15 mutant strains in Guy11, pBV591-carrying and histone H1-RFP parental
654 backgrounds; GL constructed the RIM15-GFP vector; ROR generated the Δ asn1 mutant strain carrying
655 pBV591; ZG characterized Δ asn1 expressing Pwl2-mCherry^{NLS} and Bas4-GFP, constructed the GFP-
656 ATG8 vector and generated strains expressing Rim15-GFP and GFP-Atg8; GL and ZG performed all the
657 microscopy; GL performed immunoblot analyses; GL generated material for RNAseq analysis and
658 performed all bioinformatic analyses; ND generated material for proteomic, phosphoproteomic and
659 metabolomic analyses. GL composed the figure panels with input from ZG. RAW wrote the manuscript
660 and finalized the figures, with contributions from all authors.

661 Competing interests

662 The authors declare no competing interests.

663 **Data availability**

664 Data supporting the findings of this study are available from the corresponding author upon request. The
665 RNAseq data described in this study will be submitted to an appropriate archive. Mutant strains generated
666 during the course of this study are available from the corresponding author upon request and with an
667 appropriate APHIS permit.

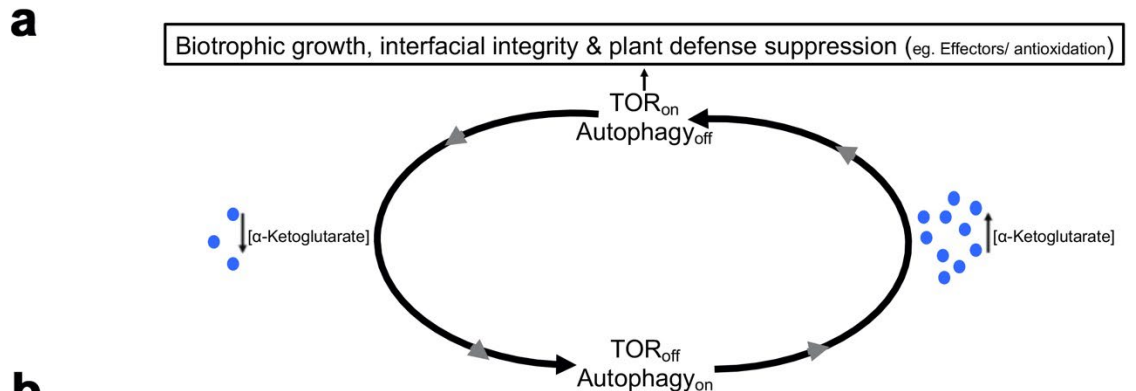
668 **References**

- 669 1. Wilson, R. A. *Magnaporthe oryzae*. *Trends Microbiol.* **29**, 663-664 (2021).
- 670 2. Wilson, R. A. & Talbot, N. J. Under pressure: investigating the biology of plant infection by
671 *Magnaporthe oryzae*. *Nat. Rev. Microbiol.* **7**, 185-95 (2009).
- 672 3. Fernandez, J. & Orth, K. Rise of a Cereal Killer: The Biology of *Magnaporthe oryzae* Biotrophic Growth.
673 *Trends Microbiol.* **26**, 582-597 (2018).
- 674 4. Cruz-Mireles, N., Eseola, A. B., Osés-Ruiz, M., Ryder, L. S. & Talbot, N. J. From appressorium to
675 transappressorium-Defining the morphogenetic basis of host cell invasion by the rice blast fungus. *PLoS*
676 *Pathog.* **17**, e1009779 (2021).
- 677 5. Yi, M. & Valent, B. Communication between filamentous pathogens and plants at the biotrophic
678 interface. *Annu. Rev. Phytopathol.* **51**, 587-611 (2013).
- 679 6. Khang, C. H. et al. Translocation of *Magnaporthe oryzae* effectors into rice cells and their subsequent
680 cell-to-cell movement. *Plant Cell* **22**, 1388-1403 (2010).
- 681 7. Giraldo MC et al. Two distinct secretion systems facilitate tissue invasion by the rice blast fungus
682 *Magnaporthe oryzae*. *Nat. Commun.* **4**, 1996 (2013).
- 683 8. Huang, K., Czymbek, K. J., Caplan, J. L., Sweigard, J. A. & Donofrio, N. M. HYR1-mediated
684 detoxification of reactive oxygen species is required for full virulence in the rice blast fungus. *PLoS*
685 *Pathog.* **7**, e1001335 (2011).
- 686 9. Marroquin-Guzman, M. et al. The *Magnaporthe oryzae* nitrooxidative stress response suppresses rice
687 innate immunity during blast disease. *Nat. Microbiol.* **2**, 17054 (2017).
- 688 10. Li, G. et al. Terminating rice innate immunity induction requires a network of antagonistic and redox-
689 responsive E3 ubiquitin ligases targeting a fungal sirtuin. *New Phytol.* **226**, 523-540 (2020).
- 690 11. Rocha, R. O. & Wilson, R. A. *Magnaporthe oryzae* nucleoside diphosphate kinase is required for
691 metabolic homeostasis and redox-mediated host innate immunity suppression. *Mol. Microbiol.* **114**, 789-
692 807 (2020).

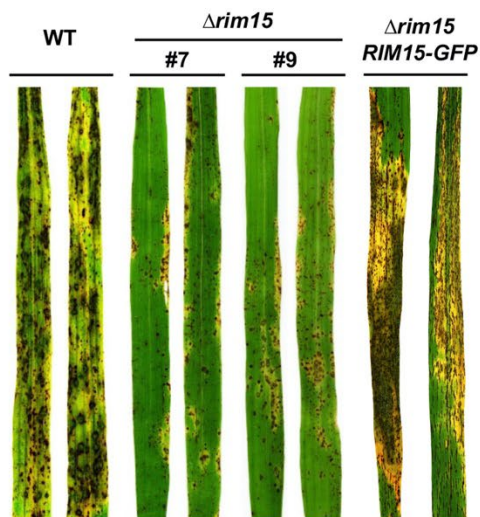
- 693 12. Kankanala, P., Czymbek, K. & Valent, B. Roles for rice membrane dynamics and plasmodesmata
694 during biotrophic invasion by the blast fungus. *Plant Cell* **19**, 706-724 (2007).
- 695 13. Sun, G., Elowsky, C., Li, G. & Wilson RA. TOR-autophagy branch signaling via Imp1 dictates plant-
696 microbe biotrophic interface longevity. *PLoS Genet.* **14**, e1007814 (2018).
- 697 14. Wilson, R. A. et al. Towards defining nutrient conditions encountered by the rice blast fungus during
698 host infection. *PLoS One* **7**, e47392 (2012).
- 699 15. Fernandez, J., Yang, K. T., Cornwell, K. M., Wright, J. D. & Wilson, R. A. Growth in rice cells requires
700 de novo purine biosynthesis by the blast fungus *Magnaporthe oryzae*. *Sci. Rep.* **3**, 2398 (2013).
- 701 16. Marroquin-Guzman, M., Krotz, J., Appeah, H. & Wilson, R. A. Metabolic constraints on *Magnaporthe*
702 biotrophy: loss of *de novo* asparagine biosynthesis aborts invasive hyphal growth in the first infected rice
703 cell. *Microbiology* **164**, 1541–1546 (2018).
- 704 17. Loewith, R. & Hall, M. N. Target of rapamycin (TOR) in nutrient signaling and growth control. *Genetics*
705 **189**, 1177-1201 (2011).
- 706 18. Swinnen, E. et al. Rim15 and the crossroads of nutrient signalling pathways in *Saccharomyces*
707 *cerevisiae*. *Cell Div.* **1**, 3 (2006).
- 708 19. Yorimitsu, T., Zaman, S., Broach, J. R. & Klionsky, D. J. Protein kinase A and Sch9 cooperatively
709 regulate induction of autophagy in *Saccharomyces cerevisiae*. *Mol. Biol. Cell* **18**, 4180-4189 (2007).
- 710 20. Yang, Z., Geng, J., Yen, W. L., Wang, K. & Klionsky, D. J. Positive or negative roles of different cyclin-
711 dependent kinase Pho85-cyclin complexes orchestrate induction of autophagy in *Saccharomyces*
712 *cerevisiae*. *Mol. Cell* **38**, 250-264 (2010).
- 713 21. Kim, B., Lee, Y., Choi, H. & Huh, W. K. The trehalose-6-phosphate phosphatase Tps2 regulates
714 ATG8 transcription and autophagy in *Saccharomyces cerevisiae*. *Autophagy* **17**, 1013-1027 (2021).
- 715 22. Dean, R. A. et al. The genome sequence of the rice blast fungus *Magnaporthe grisea*. *Nature* **434**,
716 980-986 (2005).
- 717 23. Valent, B., Farrall, L. & Chumley, F. G. *Magnaporthe grisea* genes for pathogenicity and virulence
718 identified through a series of backcrosses. *Genetics* **127**, 87-101 (1991).
- 719 24. Sakulkoo,W. et al. A single fungal MAP kinase controls plant cell-to-cell invasion by the rice blast
720 fungus. *Science* **359**, 1399-1403 (2018).
- 721 25. Klionsky DJ et al. Guidelines for the use and interpretation of assays for monitoring autophagy.
722 *Autophagy* **8**, 445-544 (2020).

- 723 26. Pedruzzi, I. et al. TOR and PKA signaling pathways converge on the protein kinase Rim15 to control
724 entry into G0. *Mol. Cell* **12**, 1607-1613 (2003).
- 725 27. Wanke, V. et al. Caffeine extends yeast lifespan by targeting TORC1. *Mol. Microbiol.* **69**, 277-285
726 (2008).
- 727 28. Saunders, D. G., Aves, S. J. & Talbot, N.J. Cell cycle-mediated regulation of plant infection by the rice
728 blast fungus. *Plant Cell* **22**, 497-507 (2010).
- 729 29. Mora, J. Glutamine metabolism and cycling in *Neurospora crassa*. *Microbiol. Rev.* **54**, 293-304 (1990).
- 730 30. Fernandez, J., Marroquin-Guzman, M. & Wilson, R. A. Evidence for a transketolase-mediated
731 metabolic checkpoint governing biotrophic growth in rice cells by the blast fungus *Magnaporthe oryzae*.
732 *PLoS Pathog.* **10**, e1004354 (2014).
- 733 31. May, A. I., Prescott, M. & Ohsumi, Y. Autophagy facilitates adaptation of budding yeast to respiratory
734 growth by recycling serine for one-carbon metabolism. *Nat. Commun.* **11**, 5052 (2020).
- 735 32. Durán, R.V. et al. Glutaminolysis activates Rag-mTORC1 signaling. *Mol. Cell.* **47**, 349-358 (2012).
- 736 33. Tan, H. W. S., Sim, A. Y. L., Long, Y. C. Glutamine metabolism regulates autophagy-dependent
737 mTORC1 reactivation during amino acid starvation. *Nat. Commun.* **8**, 338 (2017).
- 738 34. Natarajan, K. et al. Transcriptional profiling shows that Gcn4p is a master regulator of gene
739 expression during amino acid starvation in yeast. *Mol. Cell Biol.* **21**, 4347-4368 (2001).
- 740 35. Tallóczy, Z. et al. Regulation of starvation- and virus-induced autophagy by the eIF2 α kinase signaling
741 pathway. *Proc. Natl. Acad. Sci. U. S. A.* **99**, 190-195 (2002).
- 742 36. Mitta, N. et al. The Gcn4 transcription factor reduces protein synthesis capacity and extends yeast
743 lifespan. *Nat. Commun.* **8**, 457 (2017).
- 744 37. Delorme-Axford, E. & Klionsky, D. J. Transcriptional and post-transcriptional regulation of autophagy
745 in the yeast *Saccharomyces cerevisiae*. *J. Biol. Chem.* **293**, 5396-5403 (2018).
- 746 38. Srinivasan, R., Walvekar, A. S., Rashida, Z., Seshasayee, A. & Laxman, S. Genome-scale
747 reconstruction of Gcn4/ATF4 networks driving a growth program. *PLoS Genet.* **16**, e1009252 (2020).
- 748 39. Chaloner, T. M., Gurr, S. J. & Bebb, D. P. Plant pathogen infection risk tracks global crop yields
749 under climate change. *Nat. Clim. Chang.* **11**, 710–715 (2021)

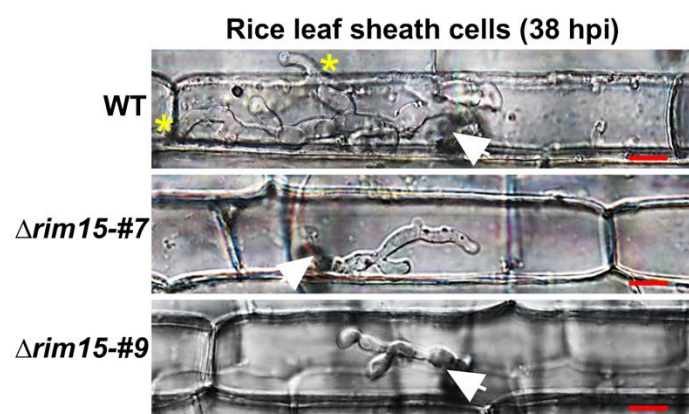
- 750 40. Li, G., Marroquin-Guzman, M. & Wilson, R. A. Chromatin Immunoprecipitation (ChIP) Assay for
751 Detecting Direct and Indirect Protein – DNA Interactions in *Magnaporthe oryzae*. *Bio-protocol* **5**, e1643
752 (2015).
- 753 41. Martin, M. Cutadapt removes adapter sequences from high-throughput sequencing reads.
754 *EMBnet.journal* **17**, 10-12 (2011).
- 755 42. Liao, Y., Smyth, G. K. & Shi, W. The Subread aligner: fast, accurate and scalable read mapping by
756 seed-and-vote. *Nucleic Acids Res.* **41**, e108 (2013).
- 757 43. Liao, Y., Smyth, G. K. & Shi, W. featureCounts: an efficient general purpose program for assigning
758 sequence reads to genomic features. *Bioinformatics* **30**, 923-30 (2014).
- 759 44. Love, M. I., Huber, W. & Anders, S. Moderated estimation of fold change and dispersion for RNA-seq
760 data with DESeq2. *Genome Biol.* **15**, 550 (2014).
- 761 45. Wickham, H. *ggplot2: Elegant Graphics for Data Analysis* (Springer, Berlin, 2009).
- 762 46. Jarabo, A., Buisan, R. & Gutierrez, D. Bidirectional clustering for scalable VPL-based global
763 illumination. In: *Spanish Computer Graphics Conference*, eds: Moreno, J. L. & Sber, M., pp. 1–9
764 (Eurographics Association, 2015).
- 765 47. Draisma, J., Horobet, E., Ottaviani, G., Sturmfels, B. & Thomas, R. R. The Euclidean Distance Degree
766 of an Algebraic Variety. *Found. Comput. Math.* **16**, 99–149 (2016).
- 767 48. Kolde R. Pheatmap: Pretty Heatmaps. *R package version* [https://cran.r-](https://cran.r-project.org/web/packages/pheatmap/index.html)
768 [project.org/web/packages/pheatmap/index.html](https://cran.r-project.org/web/packages/pheatmap/index.html) (2015).
- 769 49. Ashburner, M. et al. Gene ontology: tool for the unification of biology. The Gene Ontology Consortium.
770 *Nat Genet.* **25**, 25-29 (2000).
- 771 50. Kanehisa, M. & Goto, S. KEGG: kyoto encyclopedia of genes and genomes. *Nucleic Acids Res.* **28**,
772 27-30 (2000).
- 773 51. Huang, da W., Sherman, B T. & Lempicki, R. A. Systematic and integrative analysis of large gene
774 lists using DAVID bioinformatics resources. *Nat. Protoc.* **4**, 44-57 (2009a).
- 775 52. Huang, da W., Sherman, B. T. & Lempicki, R. A. Bioinformatics enrichment tools: paths toward the
776 comprehensive functional analysis of large gene lists. *Nucleic Acids Res.* **37**, 1-13 (2009b).
- 777 53. Taus, T. et al. Universal and confident phosphorylation site localization using phosphoRS. *J.*
778 *Proteome Res.* **10**, 5354-5362 (2011).



b

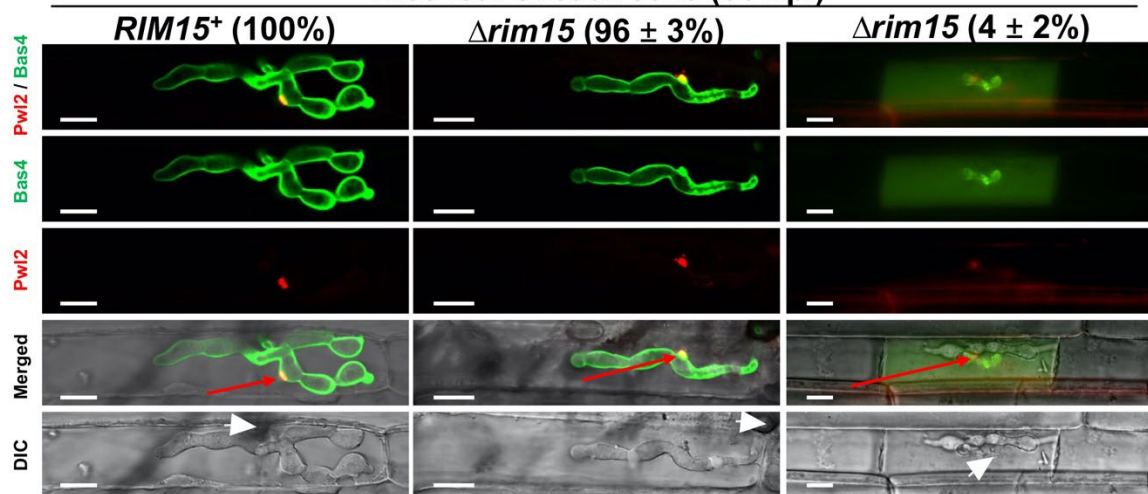


c



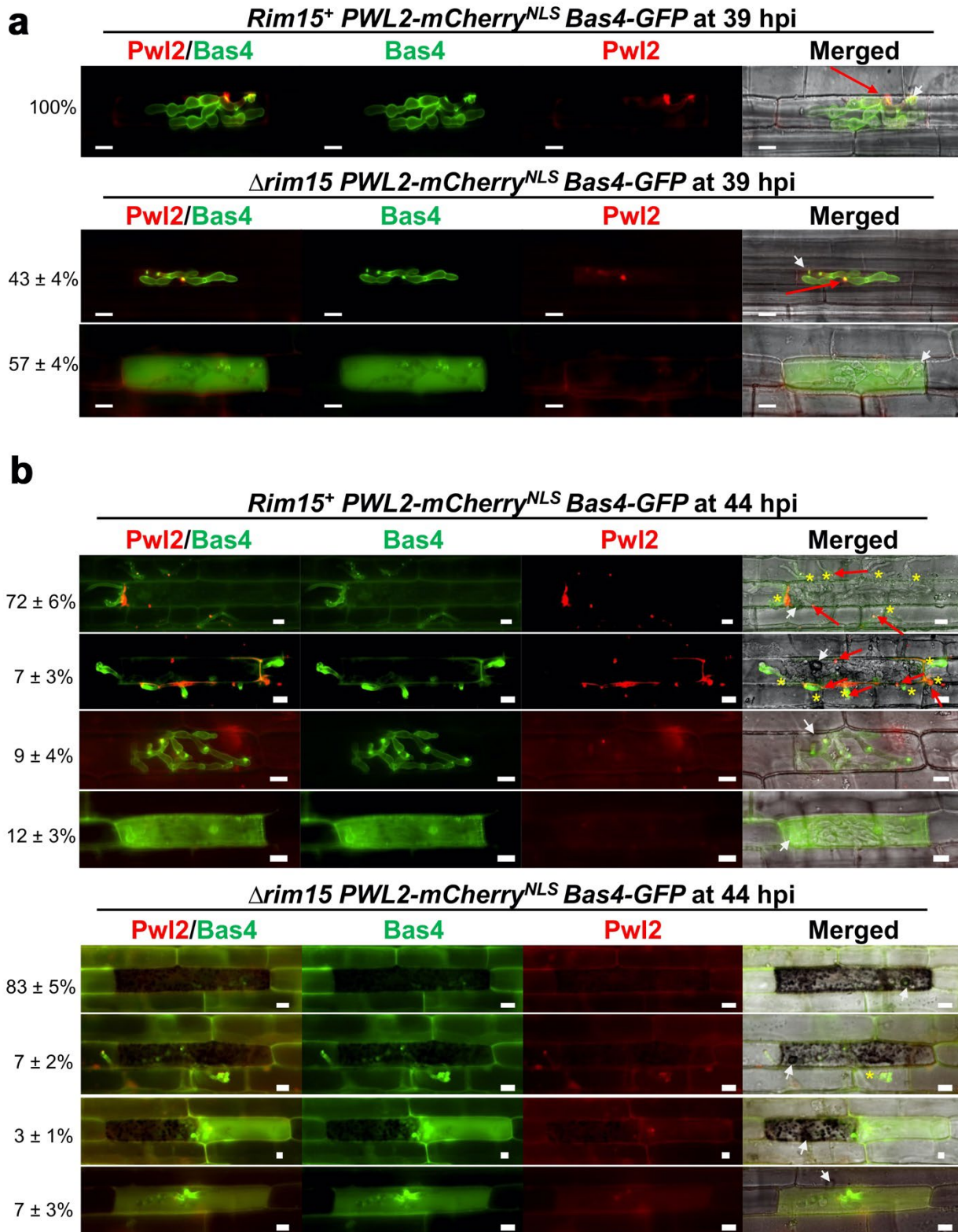
d

Rice leaf sheath cells (36 hpi)



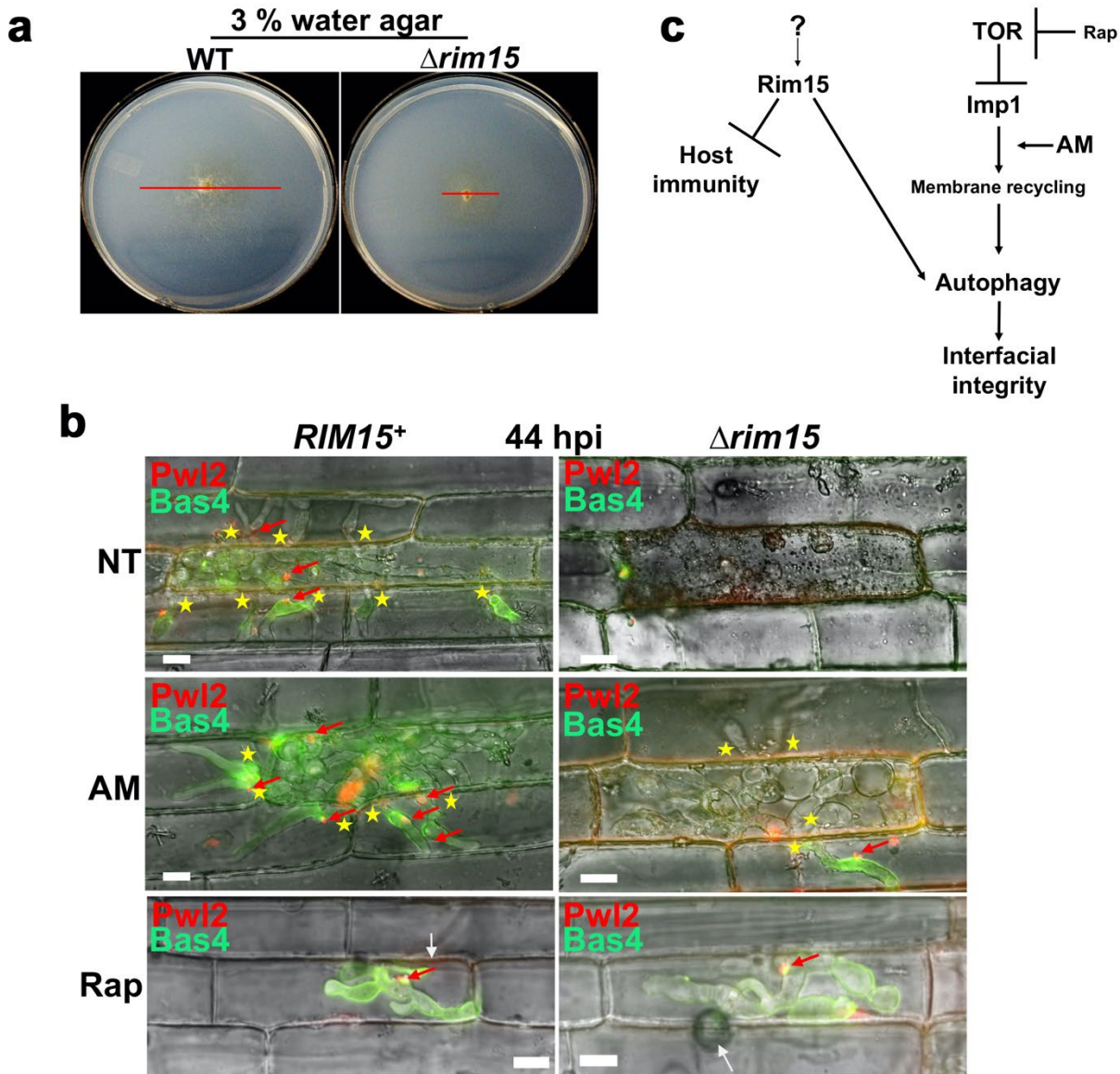
782 strains. Spores applied to 3-week-old rice seedlings of the susceptible cultivar CO-39 at a rate of 1×10^5
783 spores ml⁻¹. Images were taken at 120 hr post inoculation (hpi). **c.** Live-cell imaging at 38 hpi of detached
784 rice leaf sheaths infected with the indicated strains showing how $\Delta rim15$ strains are impaired for
785 biotrophic growth. White arrows indicate appressorial penetration sites. Asterisks indicate movement of IH
786 into neighbouring cells. Scale bar is 10 μ m. **d.** Live-cell imaging at 36 hpi of detached rice leaf sheaths
787 infected with strains expressing Pwl2-mCerry^{NLS} and Bas4-GFP shows how biotrophic membranes were
788 intact in most rice cells (96 %) infected with the $\Delta rim15$ mutant strain, but for a small subset (4 %),
789 interfacial erosion is visible. White arrowheads indicate appressorial penetration sites. Red arrows
790 indicate BICs in the merged channel for ease of viewing. Representative images and values are derived
791 from observing 50 infected rice cells per strain, repeated in triplicate. Values are averages with standard
792 deviation. DIC is differential interference contrast. Scale bar is 10 μ m.

793



795 **Figure 2. Loss of *RIM15* results in biotrophic interface erosion and the induction of strong plant
796 defense responses.** Live-cell imaging at 39 hpi (**a**) and 44 hpi (**b**) of detached rice leaf sheaths infected
797 with strains expressing Pwl2-mCerry^{NLS} and Bas4-GFP shows how $\Delta rim15$ biotrophic membranes erode
798 over time. This membrane loss is accompanied by the induction of severe host plant cell responses that
799 are not observed for *RIM15*⁺-infected rice cells at these time points. White arrows indicate appressorial
800 penetration sites. Red arrows denote BICs. Asterisks indicate movement of IH into neighbouring cells.
801 Representative images and values are derived from observing 50 infected rice cells per strain, repeated
802 in triplicate. Values are averages with standard deviation. Scale bar is 10 μm .

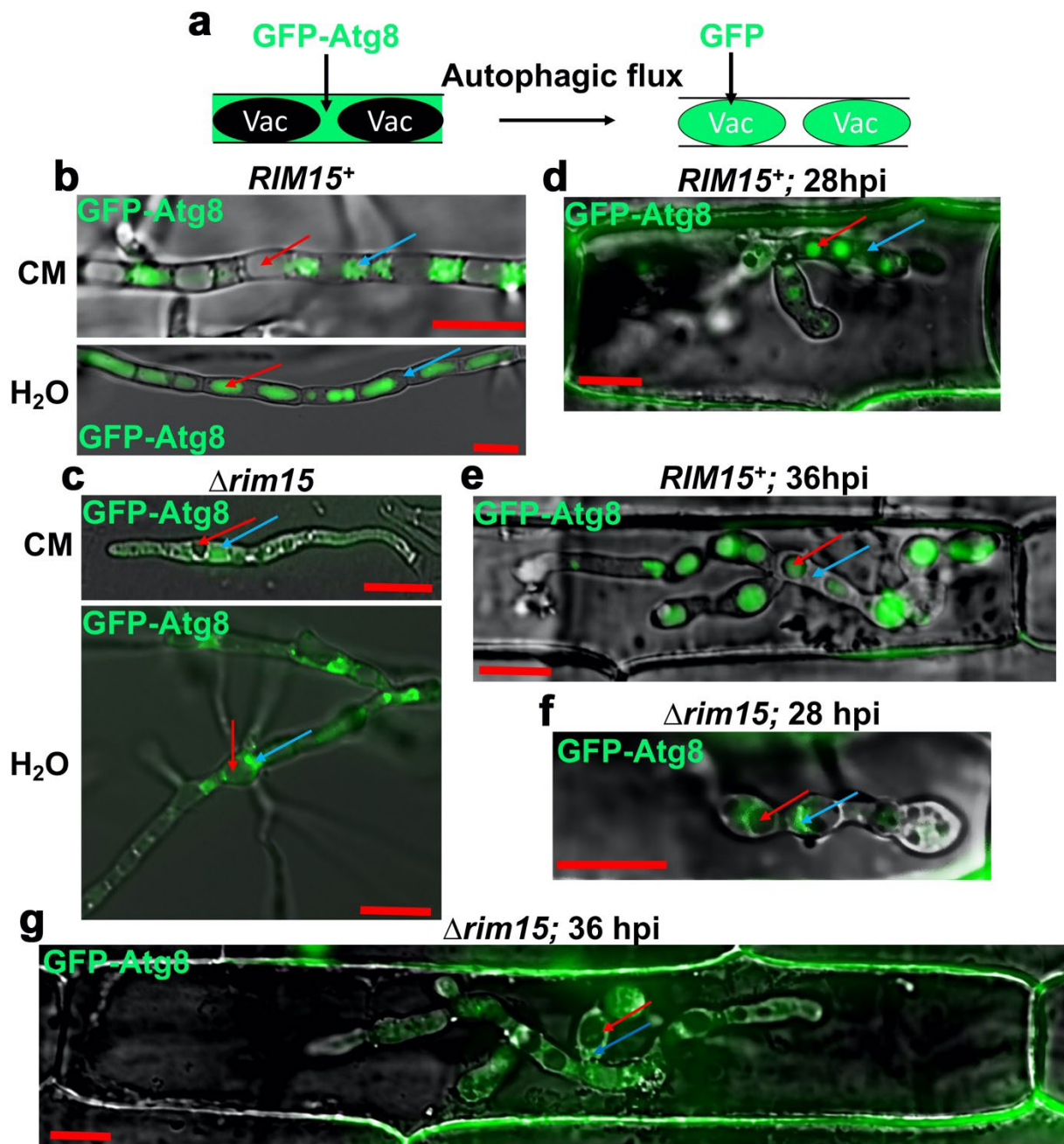
803



805 **Figure 3. *RIM15* acts on autophagy in parallel with the TOR-Imp1-autophagy pathway.** **a.** Plate tests
 806 showing impaired growth of the $\Delta rim15$ mutant strain on 3 % water agar media without nutrients,
 807 compared to WT. Red bar indicates colony diameters. Images were taken at 12 dpi. **b.** Live-cell imaging
 808 of detached rice leaf sheaths infected with strains expressing Pwi2-mCherry^{NLS} and Bas4-GFP shows
 809 how amiodarone hydrochloride (AM) and rapamycin (Rap) treatment both remediated $\Delta rim15$ biotrophic
 810 interfacial membrane integrity. AM but not rap treatment remediated $\Delta rim15$ IH growth to adjacent cells.
 811 Leaf sheaths were treated with 1.5 μ M AM or 10 μ M Rap dissolved in 1% DMSO at 36 hpi and viewed at
 812 44 hpi. White arrows indicate appressorial penetration sites. Red arrows denote BICs. Asterisks indicate
 813 movement of IH into neighbouring cells. All images are representative of 50 infected rice cells per strain,

814 repeated in triplicate. Scale bar is 10 μ m. NT is no treatment. Merged channel is shown. **c.** Model
815 showing relationship between Rim15, TOR-Imp1 signaling and autophagy.

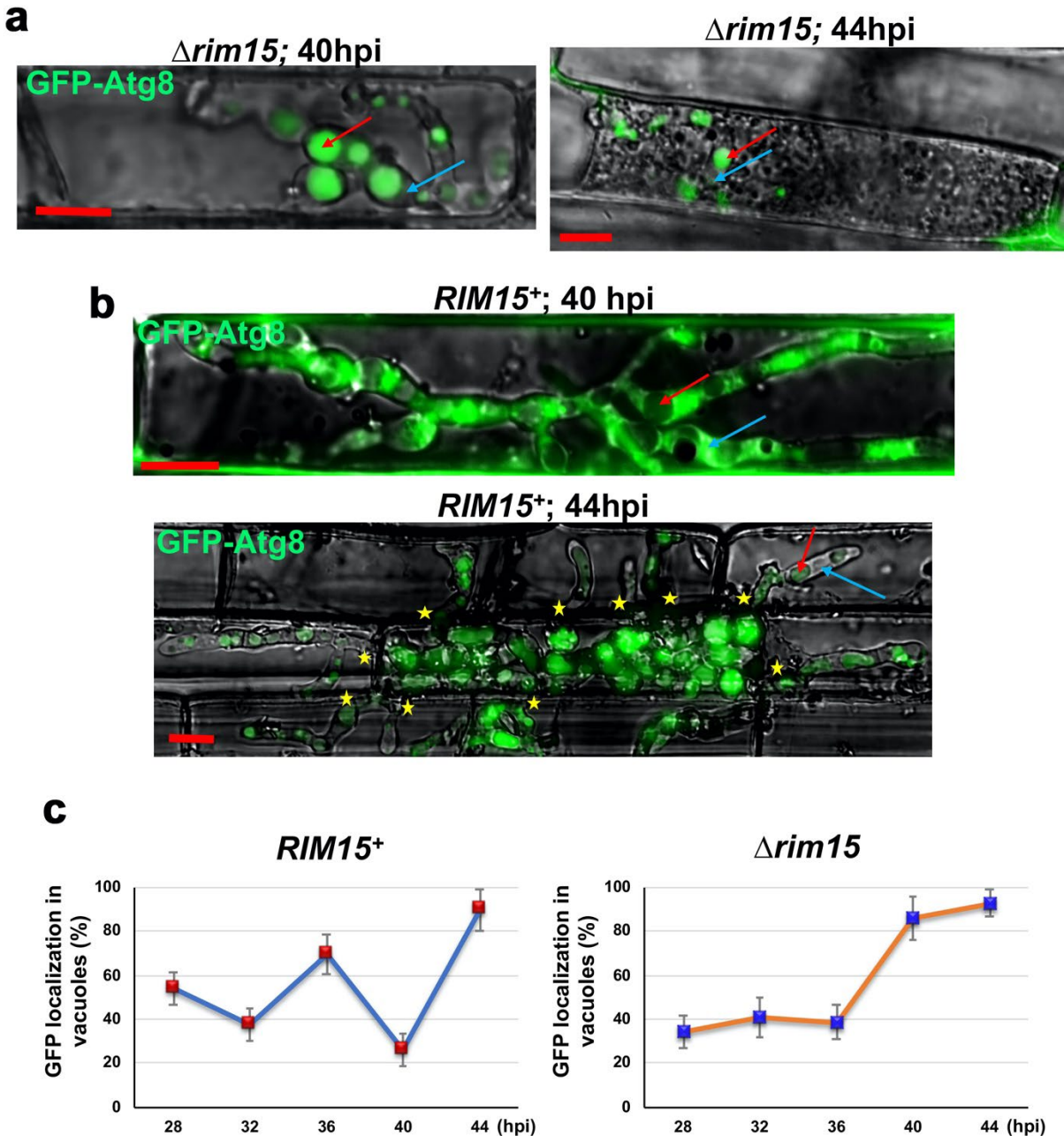
816



818 **Figure 4. Rim15 is required for autophagic flux in vegetative hyphae and IH.** **a.** Schematic of the
 819 GFP-Atg8 bulk autophagy activity assay. Vac are vacuoles. **b-g.** Micrographs showing how autophagy
 820 activity is attenuated in $\Delta rim15$ strains compared to WT. Examples of vacuoles are indicated with red
 821 arrows; examples of cytoplasm are indicated with blue arrows. Bar is 10 μm . Merged channel is shown.
 822 **b,c.** Mycelia of the indicated strains expressing GFP-Atg8 were inoculated in liquid CM medium for 42 hr
 823 before harvesting. Mycelia was washed with water and inoculated into fresh liquid CM or water, as
 824 indicated, for 3.5 hr before imaging. **d-g.** Live-cell imaging of detached rice leaf sheaths infected with

825 strains expressing GFP-Atg8 at the indicated time points. All images are representative of 50 infected rice
826 cells per strain, repeated in triplicate, and obtained using a Nikon Eclipse Ni-E upright microscope at 28
827 hpi (**d,f**) and 36 hpi (**e,g**).

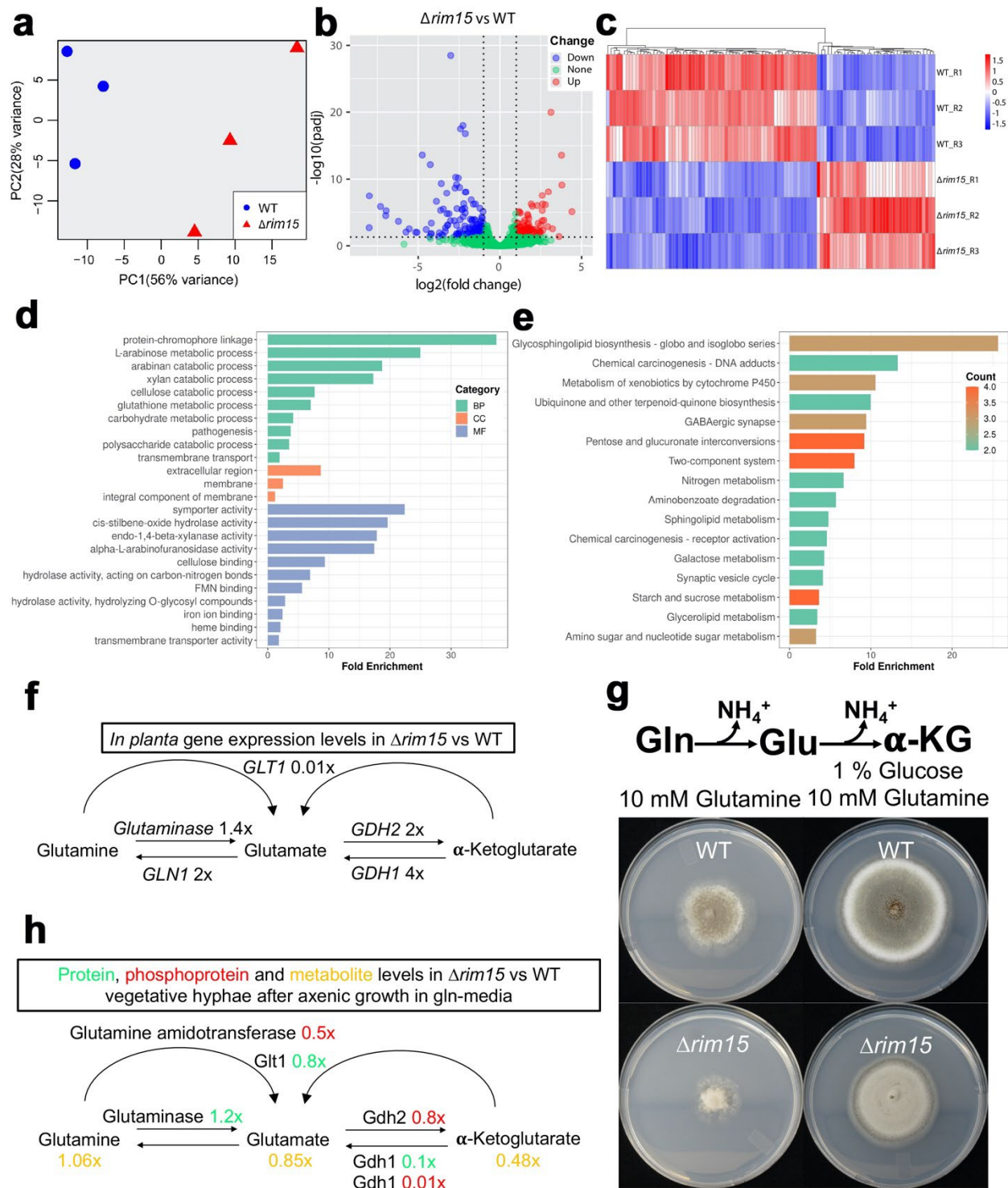
828



830 **Figure 5. Autophagic cycling in IH is Rim15-dependent.** **a,b.** Live-cell imaging of detached rice leaf
 831 sheaths infected with strains expressing GFP-Atg8 shows how in $\Delta rim15$ strains at 40 hpi and 44 hpi,
 832 autophagic flux is remediated relative to earlier time points (**a**). In contrast, in $RIM15^+$ strains, autophagic
 833 activity is reduced at 40 hpi relative to earlier time points but increases again at 44 hpi (**b**). All images are
 834 representative of 50 infected rice cells per strain, repeated in triplicate. Examples of vacuoles are
 835 indicated with red arrows; examples of cytoplasm are indicated with blue arrows. Asterisks indicate
 836 movement of IH into neighbouring cells. Bar is 10 μ m. Merged channel is shown. **b.** Quantification of GFP
 837 localization in vacuoles during IH growth shows how autophagy activity cycles in WT, but autophagic

838 cycling is abolished in $\Delta rim15$. Values are the average number of IH vacuoles accumulating GFP in 50
839 infected rice cells as a percentage of the total number of vacuoles, repeated in triplicate. Error bars are
840 standard deviation.

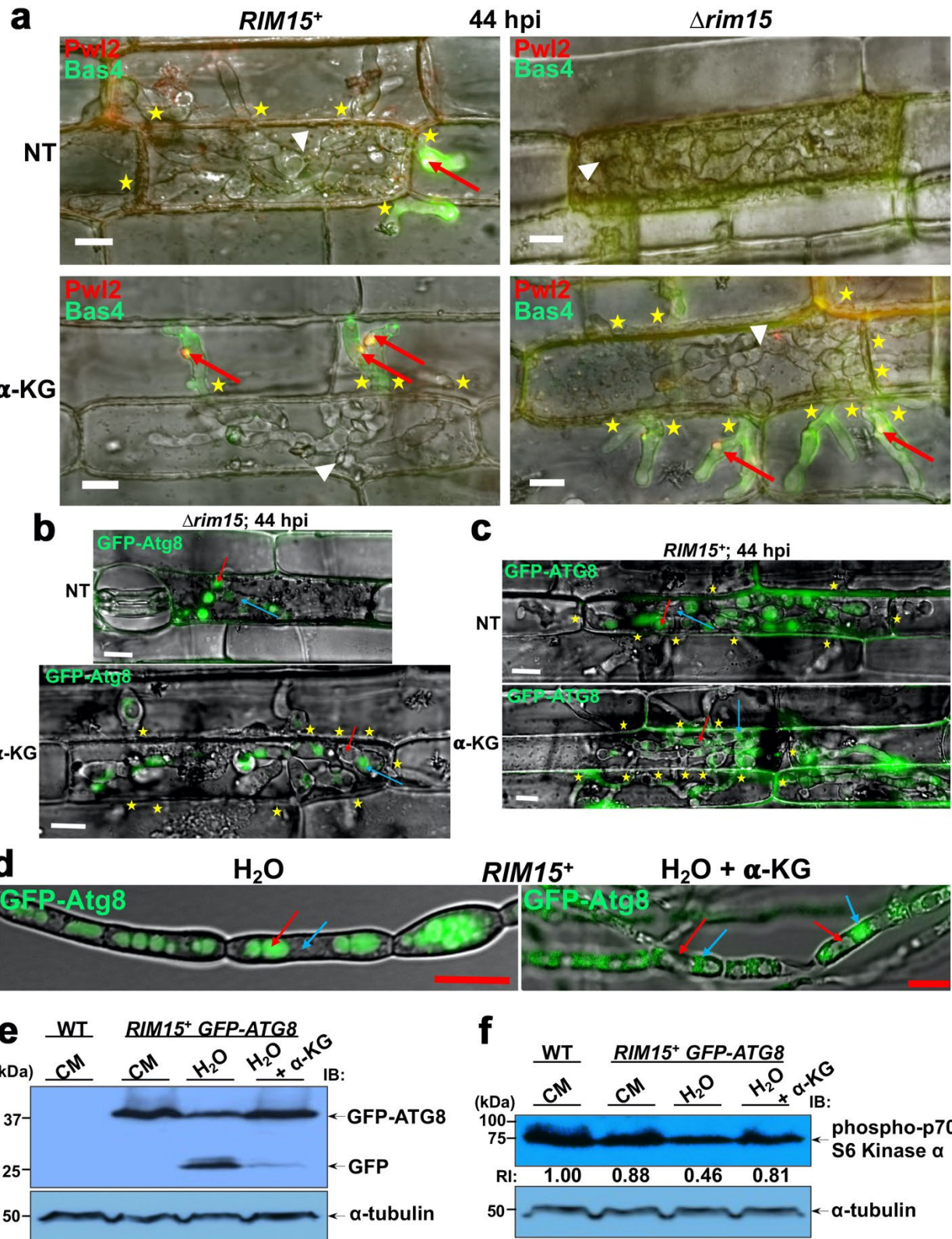
841



845 hpi compared to WT-infected leaf sheaths. **a.** Principal component analysis (PCA) plot, based on all
846 genes detected in RNA-seq analysis, indicating different *in planta* gene expression patterns between
847 $\Delta rim15$ and WT strains. **b.** Distribution and expression levels of DEGs in $\Delta rim15$ and WT IH in rice cells.
848 The x-axis represents the log₂ [Fold Change] values of all detected genes in $\Delta rim15$ versus WT strain,
849 and the y-axis represents the log-transformed adjusted p values for the differences in expression. **c.**
850 Heatmap showing the hierarchical clustering analysis of the top 100 DEGs in $\Delta rim15$ and WT strains in
851 the rice cells across all three replicates. The clustering patterns of these DEGs were determined by
852 cluster analysis using the Euclidean distance method going with the complete-linkage. Each row
853 represents a sample; each column represents a single gene. **d.** Functional classification of identified
854 DEGs in $\Delta rim15$ and WT strains *in planta* based on GO enrichment analysis. BP: biological process; CC:
855 cellular compartment; MF: molecular function. **e.** KEGG pathway enrichment analysis of DEGs in $\Delta rim15$
856 and WT strains growing in the rice cells. **d,e.** Fold Enrichment is the percentage of genes in the DEGs
857 belonging to that category or pathway, divided by the corresponding percentage in the genome. **f.**
858 Simplified schematic of the GS-GOGAT cycle summarizing RNAseq data (**Supplementary Table 1**) from
859 15 infected detached rice leaf sheaths per strain, repeated in triplicate and compared to the mock
860 infection control, showing how GS-GOGAT cycle gene expression levels in $\Delta rim15$ IH at 36 hpi are
861 misregulated compared to WT. *GLN1* (MGG_14279) encodes glutamine synthetase; *GLT1* (MGG_07187)
862 encodes glutamate synthase (GOGAT); *GDH1* (MGG_08074) encodes NADP-specific glutamate
863 dehydrogenase; *GDH2* (MGG_05247) encodes NAD-specific glutamate dehydrogenase (Mgd1)
864 (Marroquin-Guzman and Wilson, 2015). Glutaminase is encoded at MGG_07512. GS-GOGAT cycle gene
865 transcripts with equal abundances in both strains are not shown. Values are fold changes in $\Delta rim15$
866 compared to WT. **g.** Plate tests show how glutaminolysis (the use of glutamine as a carbon source) is
867 impaired in $\Delta rim15$ compared to WT. **h.** Schematic summarizing GS-GOGAT cycle-related proteomic,
868 phosphoproteomic and metabolomic data (**Supplementary Tables 4-7**), averaged from three mycelial
869 samples per strain grown in liquid minimal media with 0.5 mM glutamine as the sole carbon and nitrogen
870 source, showing how $\Delta rim15$ strains are perturbed for the GS-GOGAT cycle and glutaminolytic metabolite
871 homeostasis. Strains were grown in CM for 42 hr before switching to 0.5 mM glutamine media for 16 hr.
872 GS-GOGAT cycle enzymes with equal abundances in both strains are not shown. Values are fold
873 changes in $\Delta rim15$ relative to WT.

874

875

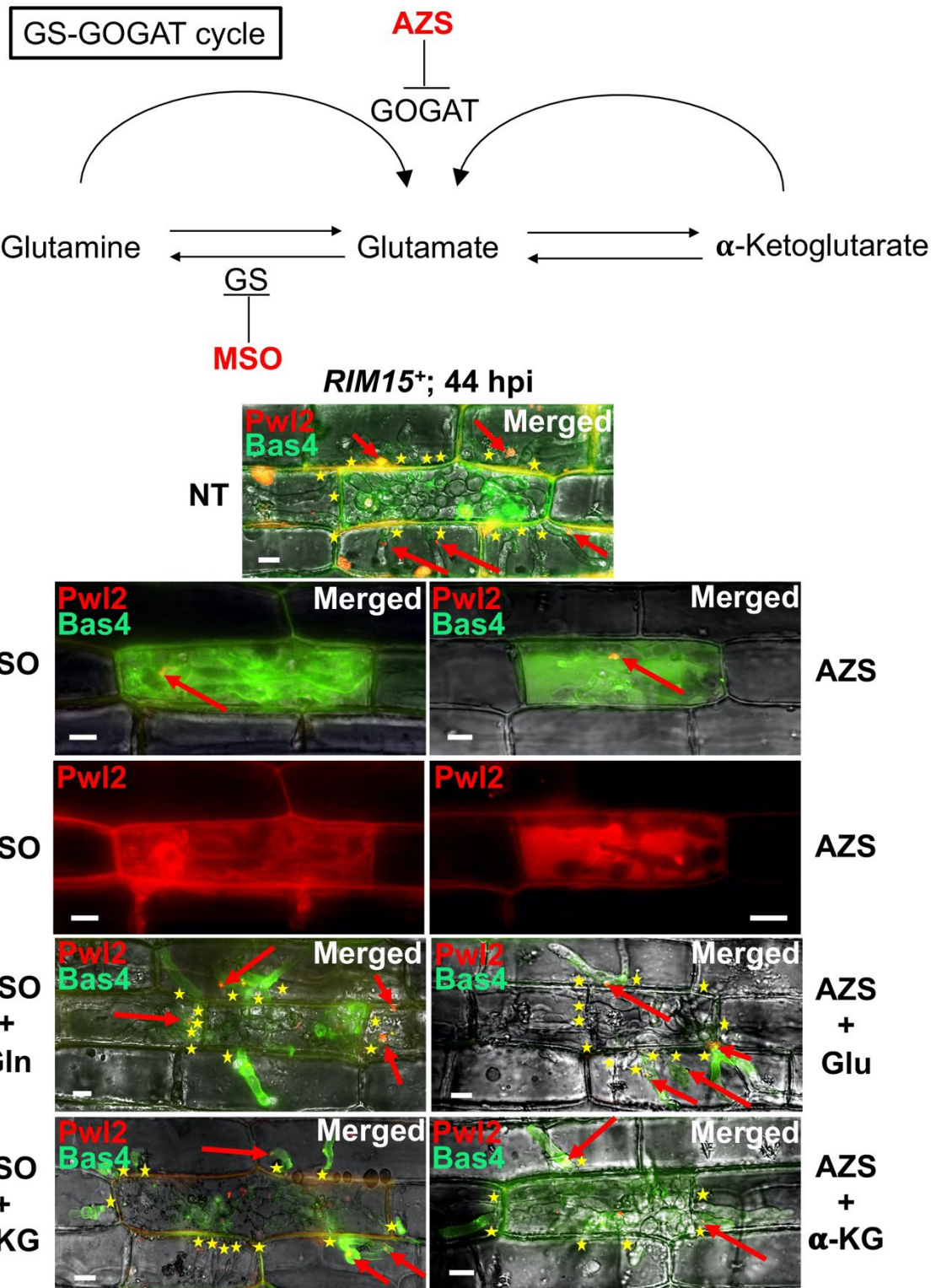


876

877 **Figure 7. α -ketoglutarate treatment remedies $\Delta rim15$ biotrophic growth defects, suppresses**878 **autophagy, and activates TOR signaling.** a. Live-cell imaging of detached rice leaf sheaths infected

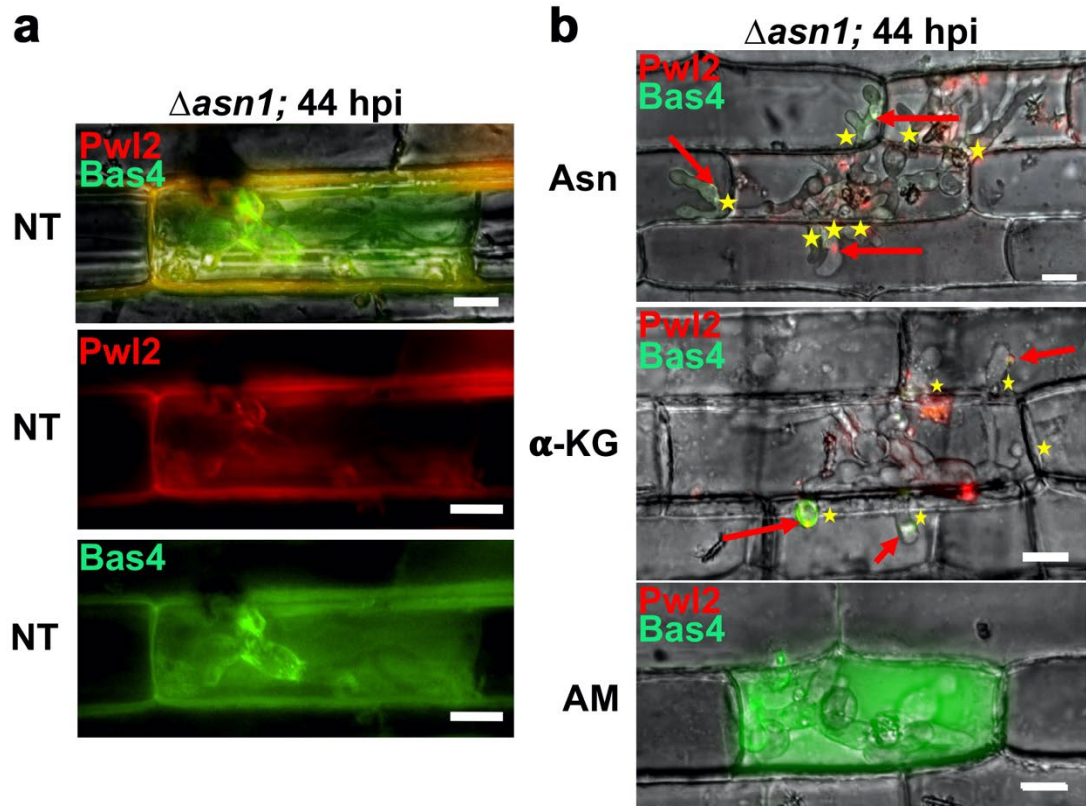
879 with strains expressing Pwl2-mCherry^{NLS} and Bas4-GFP shows how treatment with 10 mM of the α -
880 ketoglutarate (α -KG) cell-permeable analogue dimethyl α -ketoglutarate (DMKG) remediated $\Delta rim15$
881 biotrophic growth and restored biotrophic interfacial membrane integrity. White arrowheads indicate
882 appressorial penetration sites. Red arrows indicate BICs. Asterisks indicate movement of IH into
883 neighbouring cells. NT is no treatment. Bar is 10 μ m. **b,c.** Micrographs show how 10 mM α -KG treatment
884 (as DMKG) suppresses autophagy activity in $\Delta rim15$ (**b**) and WT (**c**) at 44 hpi. Examples of vacuoles are
885 indicated with red arrows; examples of cytoplasm are indicated with blue arrows. Asterisks indicate
886 movement of IH into neighbouring cells. NT is no treatment. Bar is 10 μ m. **a-c.** 10 mM α -ketoglutarate (α -
887 KG, as DMKG) was applied to detached rice leaf sheaths at 36 hpi, and images were taken at 44 hpi. All
888 images are representative of 50 infected rice cells per strain, repeated in triplicate. Merged channel is
889 shown. **d.** Micrograph showing that, although exposure to water alone for 4 hr induced autophagy in WT
890 and GFP accumulated in vacuoles, in contrast, exposure to 10 mM α -KG (as the cell-permeable DMKG
891 analogue) in water for 4 hr was sufficient to suppress autophagy, leading to GFP-Atg8 accumulation in
892 the cytoplasm. Examples of vacuoles are indicated with red arrows; examples of cytoplasm are indicated
893 with blue arrows. Bar is 10 μ m. Merged channel is shown. **e,f.** Western blots showing how, relative to CM
894 media, growth in water induced autophagic flux as evidenced by the increase in free GFP compared to
895 GFP-Atg8 monitored by the anti-GFP antibody (**e**), and suppressed TOR activity in the same strain as
896 evidenced by decreased Sch9/ p70 S6 kinase phosphorylation monitored by the anti-phospho-p70 S6
897 kinase antibody (**f**), but autophaguc flux was decreased and TOR activity increased following growth in
898 water treated with α -ketoglutarate (as DMKG). RI = relative intensity calculated by normalizing Sch9
899 phosphorylation levels determined using the anti-p-p70 S6 kinase antibody against tubulin α levels
900 determined by the anti-tubulin α antibody. (**d-f**) Mycelia were grown in liquid CM for 42 hr before switching
901 into the indicated treatments for 4 hrs.

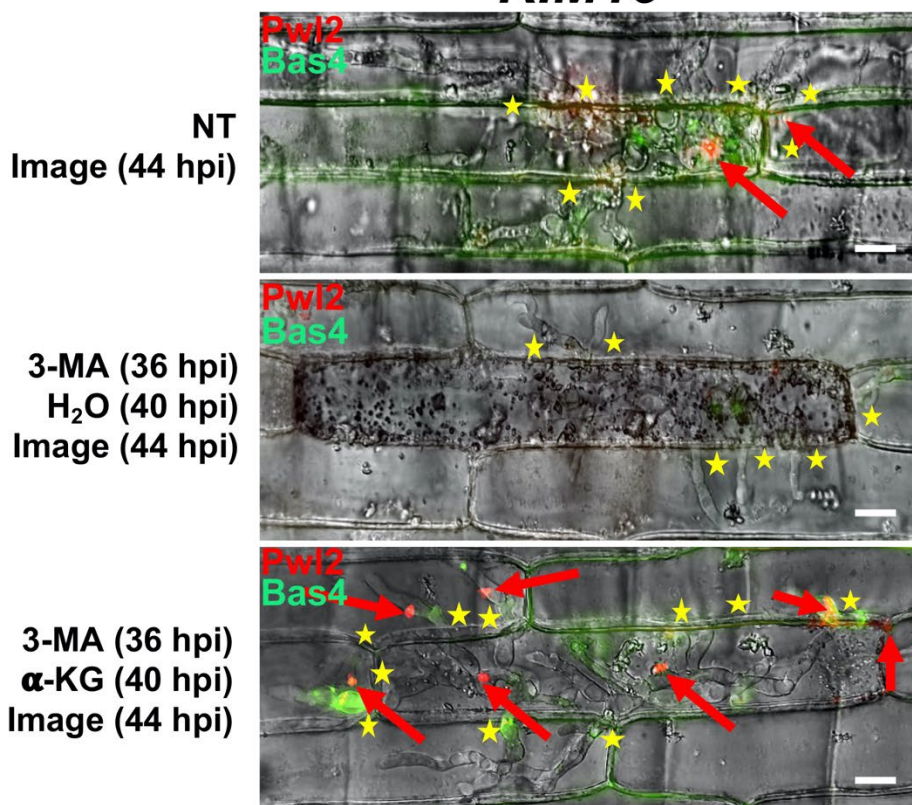
902



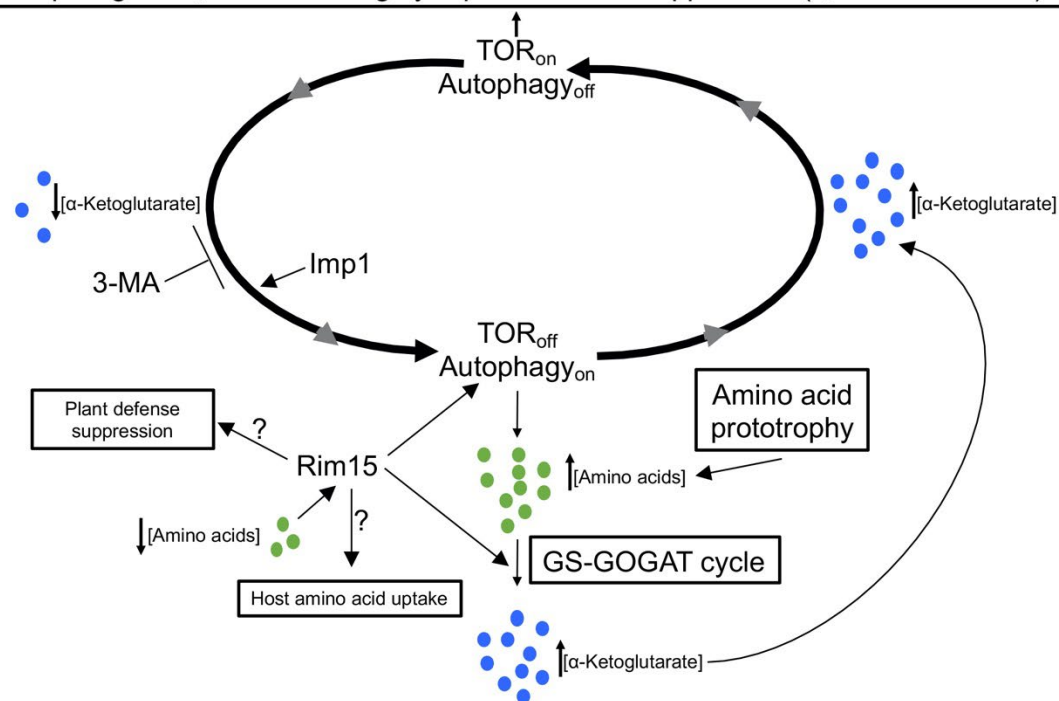
906 *RIM15*⁺-infected rice cells at 36 hpi with 1 mM L-methionine sulfoximine (MSO), the glutamine synthetase
907 inhibitor, or with 2 mM azaserine (AZS), the GOGAT inhibitor, had, by 44 hpi, abolished biotrophic growth
908 and thus phenocopied *Δrim15*. For MSO + Gln treatments, 1 mM MSO was first applied to the detached
909 rice leaf sheath at 36 hpi and then replaced by 1 mM MSO + 10 mM glutamine at 40 hpi before imaging at
910 44 hpi. For AZs + Glu and AZS + α-KG, 2 mM AZS was first applied to the detached rice leaf sheath at
911 36 hpi then replaced at 40 hpi by 2 mM AZS + 10 mM glutamate or 2 mM AZS + 10 mM α-ketoglutarate
912 (as the cell-permeable DMKG analog) before imaging at 44 hpi. All images are representative of 50
913 infected rice cells per strain, repeated in triplicate. BICs are indicated with a red arrow. Asterisks indicate
914 movement of IH into neighbouring cells. NT is no treatment. Bar is 10 μm.

915



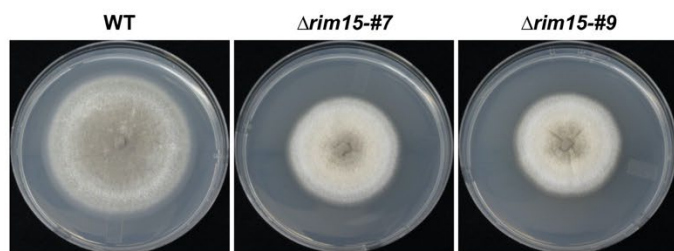
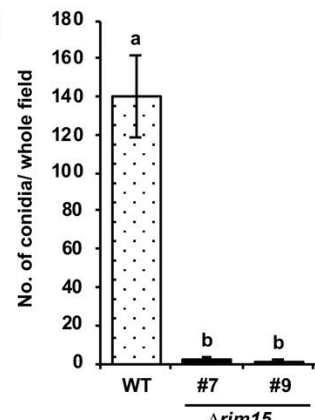
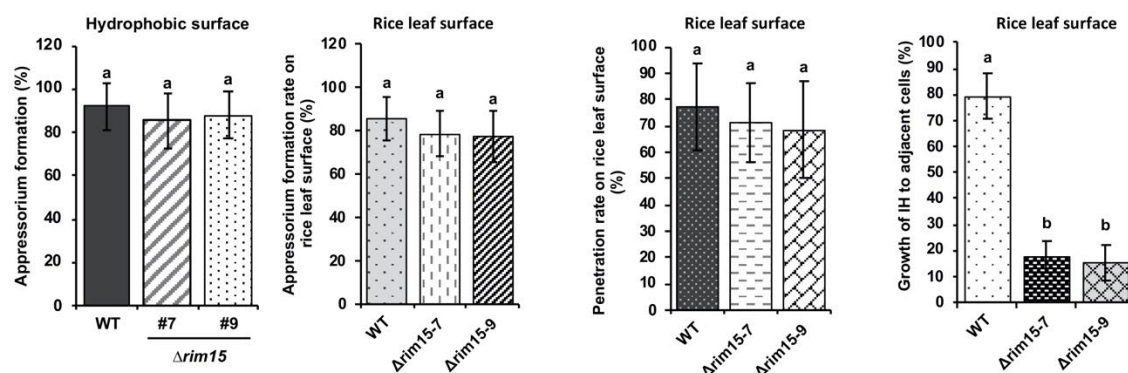
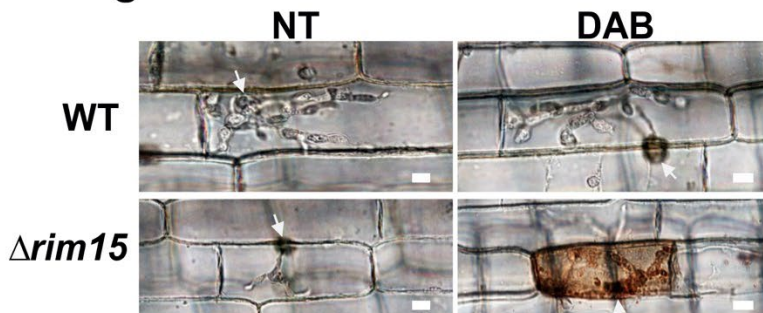
a***RIM15⁺*****b**

Biotrophic growth, interface integrity & plant defense suppression (eg. Effectors/ antioxidant)



930 autophagy blocking by 3-MA. Live cell imaging of detached rice leaf sheaths infected with WT shows how
931 α -ketoglutarate can remediate IH growth following autophagy blocking by 3-MA. Infected rice cells were
932 untreated (NT) or treated with 10 mM 3-methyladenine (3-MA) at 36 hpi before this treatment was
933 removed at 40 hpi and replaced with either water or 10 mM α -ketoglutarate (as the cell-permeable DMKG
934 analogue), as indicated, then imaged at 44 hpi. All images are representative of 50 infected rice cells per
935 strain, repeated in triplicate. Asterisks indicate movement of IH into neighbouring cells. Red arrows
936 indicate BICs. Bar is 10 μ m. Merged channel is shown. (b) Model shows how Rim15-dependent
937 autophagy activity and the GS-GOGAT cycle modulate α -ketoglutarate levels in an amino acid
938 prototrophy-dependent manner. Abundant α -ketoglutarate is an amino acid sufficiency signal to trigger
939 TOR reactivation and drive biotrophic growth. Autophagy induction (which is blocked by 3-MA) requires
940 Imp1 to facilitate phagophore expansion and membrane homeostasis¹³, as indicated. Additional roles for
941 Rim15 are postulated. See text for details.

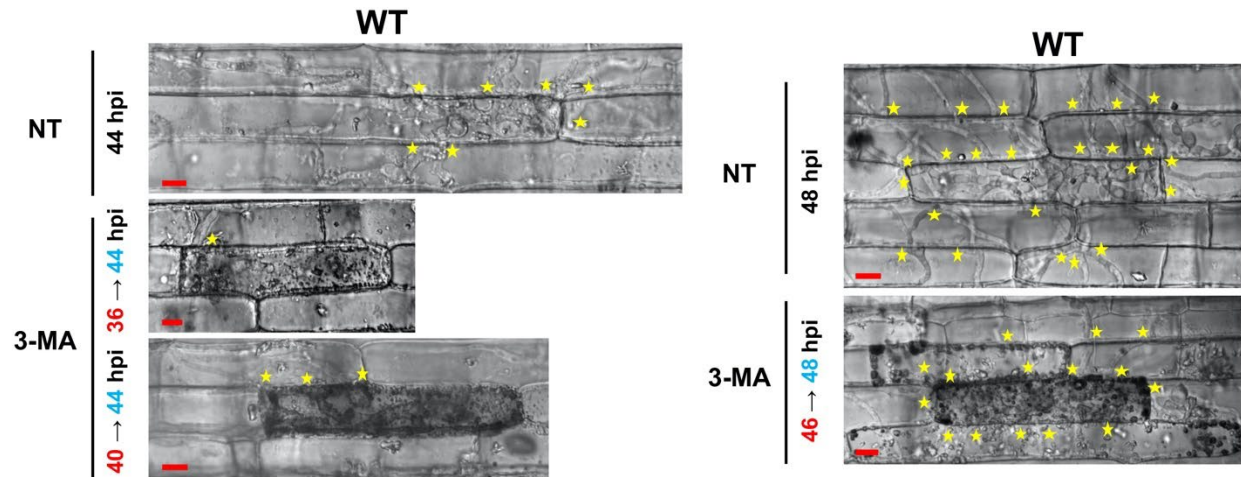
942

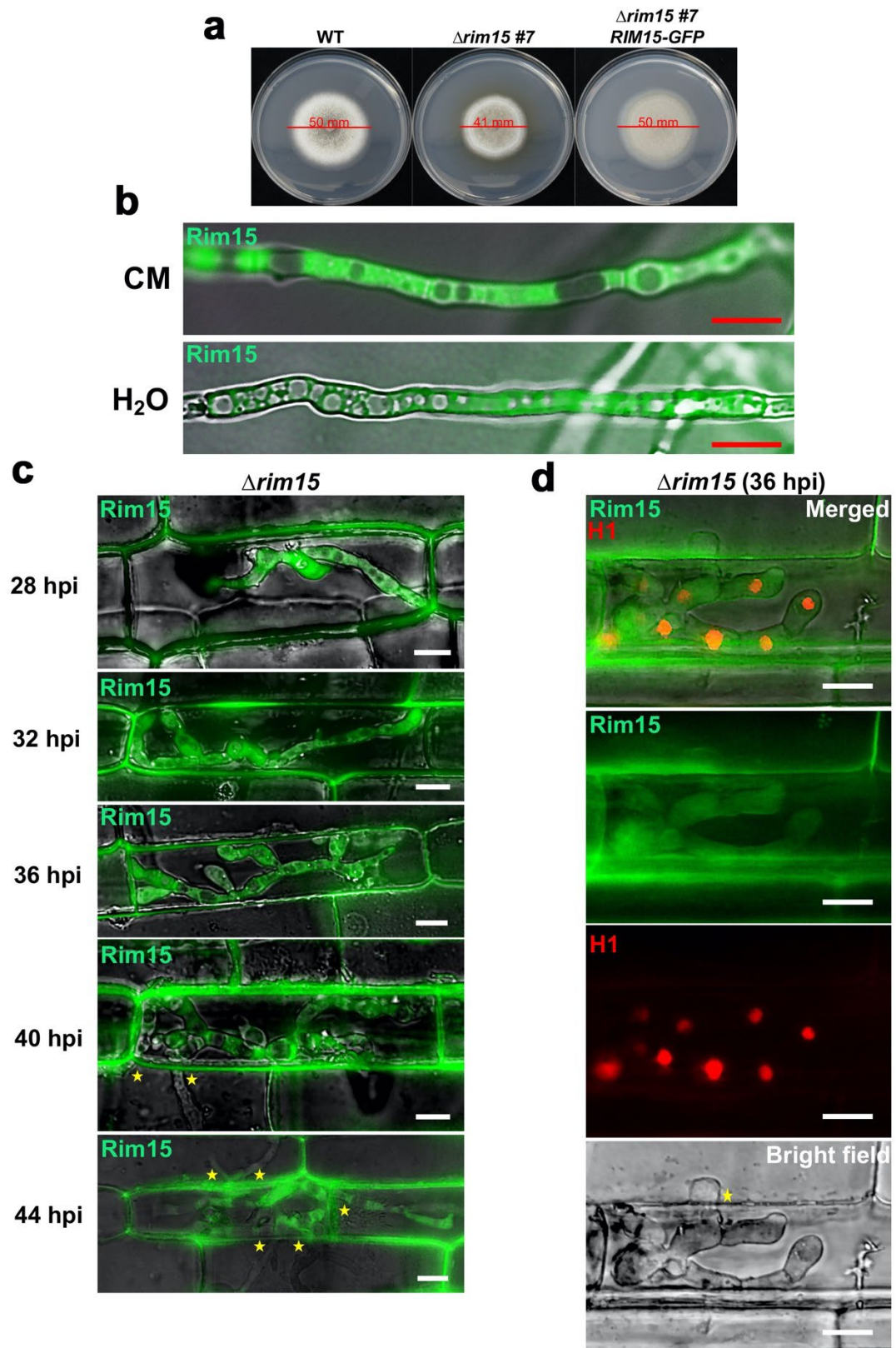
a**b****c****d****e**

948 from CM at 10 days, and the number of spores was counted using a haemocytometer under a dissecting
949 microscope. Results are the mean of three independent measurements. Error bars indicate standard
950 deviation. For each column, different letters indicate significant differences at $P \leq 0.05$ using the Student-
951 Newman-Keuls test. **c.** Loss of *RIM15* did not impair appressorium formation on artificial hydrophobic
952 surfaces. Spores were harvested from 14-day-old colonies of WT and two $\Delta rim15$ mutant strains growing
953 on oatmeal agar medium and then resuspended at 2×10^4 spores ml $^{-1}$. 200 μl of the spore suspension was
954 inoculated onto a hydrophobic plastic cover slip positioned in a humid compartment and then incubated at
955 25°C for 24 hr in the dark. Scale bar is 10 μm . Experiments were repeated in triplicate. **d.** Graphs
956 showing how appressorium formation rates on artificial hydrophobic surfaces and on rice leaf surfaces at
957 24 hpi, and appressorial penetration rates on rice leaf surfaces at 30 hpi, were not significantly ($P \leq 0.05$)
958 different between $\Delta rim15$ mutant strains and WT. However, cell-to-cell movement rates at 48 hpi were
959 significantly ($P \leq 0.05$) reduced in two independents $\Delta rim15$ mutant strains compared to WT. For
960 appressorium formation and penetration rates, 50 spores or appressoria, respectively, were observed for
961 each strain, repeated in triplicate. For IH movement rates, 50 primary infected cells were observed for
962 each strain. Values are the means of three replicates. Bars are standard deviation. Bars with the same
963 letters are not significantly different (Student's t-test, $P \leq 0.05$). **e.** Live cell-imaging of detached rice leaf
964 sheaths infected with the indicated strains shows how loss of *RIM15* elicits an oxidative burst in $\Delta rim15$ -
965 infected host rice cells. Leaf sheaths were stained with 3,3'-Diaminobenzidine (DAB) and imaged at 36
966 hpi. White arrows indicate appressorial penetration sites. All images are representative of 50 infected rice
967 cells per strain, repeated in triplicate. Scale bar is 10 μm .

968

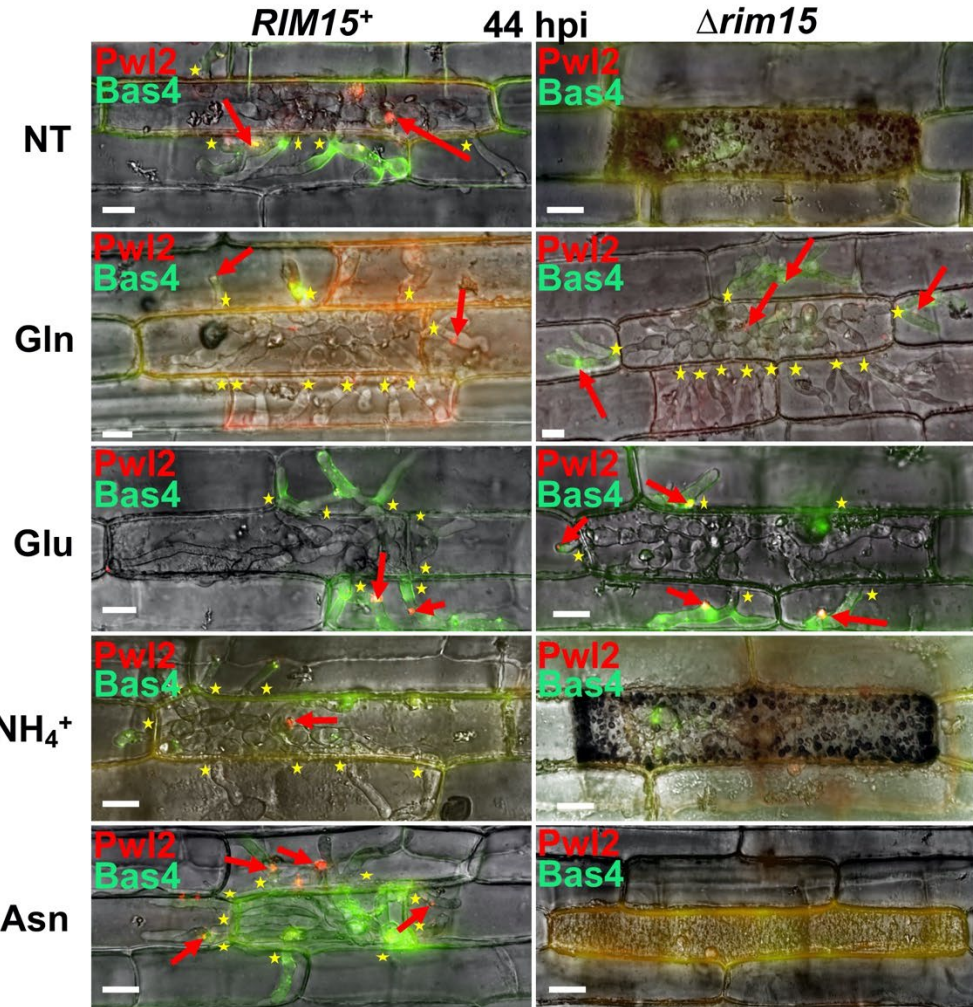
Treated at **x** hpi → viewed at **y** hpi

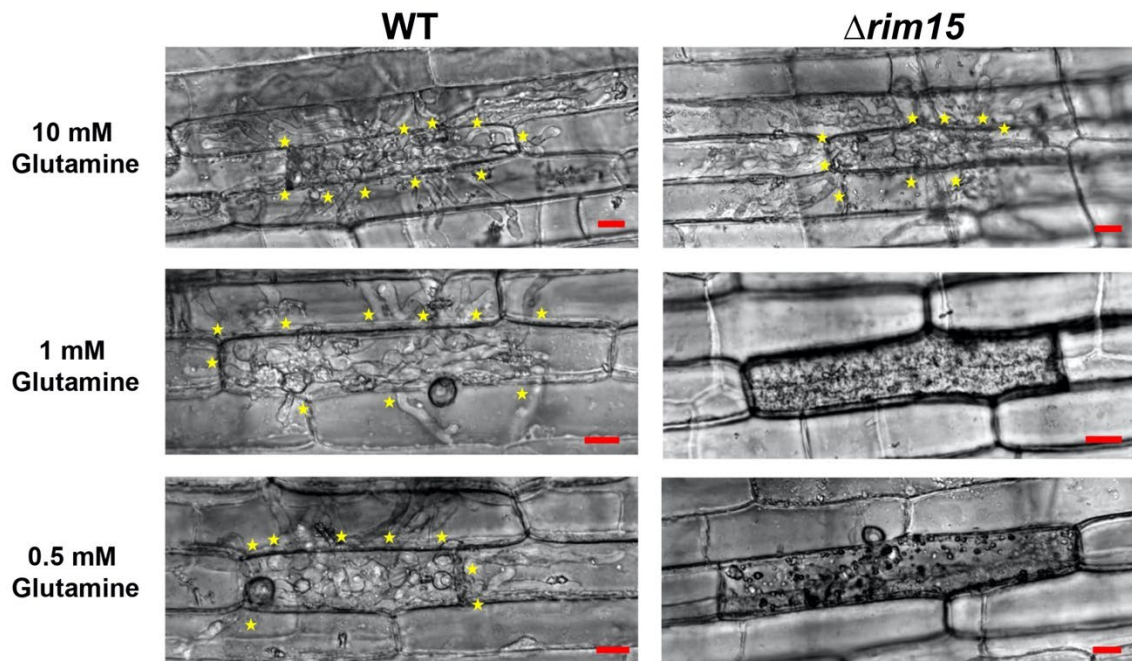




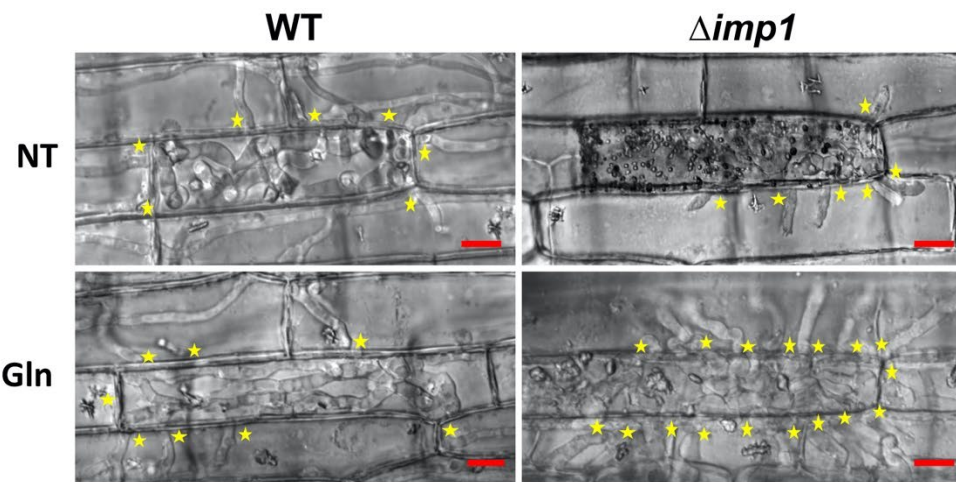
979 shows that in vegetative hyphae, Rim15-GFP remains cytoplasmic under nutrient-rich (CM) and nutrient-
980 starvation (water) culture shake conditions. The Δ *rim15 RIM15-GFP* complementation strain was grown
981 in liquid CM for 42 hr. After washing with water, vegetative hyphae were transferred into fresh liquid CM
982 or water for a further 3.5 hr before imaging. Bar is 10 μ m. Merged channel is shown. **c.** Live-cell imaging
983 at the indicated times of detached rice leaf sheaths infected with the Δ *rim15 RIM15-GFP*
984 complementation strain shows that Rim15-GFP localizes to IH cytoplasm throughout biotrophy. Asterisks
985 indicate movement of IH into neighbouring cells. Bar is 10 μ m. Merged channel is shown. **d.** Live-cell
986 imaging at 36 hpi of detached rice leaf sheaths infected with a *RIM15*⁺ strain expressing histone H1-RFP
987 and Rim15-GFP shows that Rim15-GFP does not co-localize with the nucleus. Asterisks indicate
988 movement of IH into neighbouring cells. Bar is 10 μ m.

989





1006



- 1012 **Supplementary Table 1.** RNAseq analysis by DESeq2 of differentially expressed genes in *Δrim15*-
1013 vs Guy11-infected rice leaf sheath cells at 36 hpi.
- 1014 **Supplementary Table 2.** GO enrichment analysis of differentially expressed genes in *Δrim15*- vs
1015 Guy11-infected rice leaf sheath cells at 36 hpi.
- 1016 **Supplementary Table 3.** KEGG pathway enrichment analysis of differentially expressed genes in
1017 *Δrim15*- vs Guy11-infected rice leaf sheath cells at 36 hpi.
- 1018 **Supplementary Table 4.** Proteomic analysis of protein abundances in *Δrim15* and Guy11
1019 vegetative hyphae after growth on minimal media with glutamine as a sole carbon and nitrogen
1020 source.
- 1021 **Supplementary Table 5.** Phosphoproteomic analysis of protein extracts from *Δrim15* and Guy11
1022 vegetative hyphae after growth on minimal media with glutamine as a sole carbon and nitrogen
1023 source.
- 1024 **Supplementary Table 6.** Metabolomic analysis of *Δrim15* and Guy11 vegetative hyphae after
1025 growth on minimal media with glutamine as a sole carbon and nitrogen source.
- 1026 **Supplementary Table 7.** Metabolomic analysis of *Δrim15* and Guy11 vegetative hyphae after
1027 growth on minimal media with glutamine as a sole carbon and nitrogen source.
- 1028 **Supplementary Table 8.** Strains used in this study.
- 1029 **Supplementary Table 9.** Oligonucleotide primers used in this study.

1030 **Supplementary Table 10. Plasmids used in this study.**

Supplementary Files

This is a list of supplementary files associated with this preprint. Click to download.

- [TableS1RNAseqanalysis.xlsx](#)
- [TableS2GOenrichmentanalysis.xlsx](#)
- [TableS3KEGGpathwayenrichmentanalysis.xlsx](#)
- [TableS4Proteomicdata.xlsx](#)
- [TableS5Phosphoproteomicdata.xlsx](#)
- [TableS6Metabolomicdata1.xlsx](#)
- [TableS7Metabolomicdataall.xlsx](#)
- [TableS8Strainsusedinthisstudy.xlsx](#)
- [TableS9Oligonucleotideprimersusedinthisstudy.xlsx](#)
- [TableS10Plasmidsusedinthisstudy.xlsx](#)